



INSTITUTO  
SUPERIOR  
TÉCNICO

**UNIVERSIDADE TÉCNICA DE LISBOA  
INSTITUTO SUPERIOR TÉCNICO**

# **RADAR INTERFEROMETRY: 2D PHASE UNWRAPPING VIA GRAPH CUTS**

**Gonçalo Ramiro Valadão Matias  
(Licenciado)**

Dissertação para obtenção do Grau de Mestre em  
Sistemas de Informação Geográfica

Orientador: Doutor José Manuel Bioucas Dias

## **Júri**

Presidente: Doutor Carlos Alberto Ferreira de Sousa Oliveira

Vogais: Doutor Luís Eduardo Neves Gouveia  
Doutor Mário Alexandre Teles de Figueiredo  
Doutor José Manuel Bioucas Dias  
Doutor Pedro Manuel Quintas Aguiar

**Julho de 2006**

## Abstract

Interferometric synthetic aperture radar (InSAR) is a radar remote sensing technique primarily aimed at measuring terrain altitude. Relevant InSAR features are night-and-day and all-weather operability. In particular, such features spurred InSAR based digital elevation models (DEM) into a wide spread operational use.

Phase unwrapping is the inference of absolute phase from modulo- $2\pi$  phase. This is a critical step in the InSAR processing chain, yet still one of its most challenging problems; this fact makes of phase unwrapping a crucial problem to InSAR based DEM production.

This thesis introduces a new energy minimization framework for phase unwrapping, building on graph cuts based binary optimization techniques. We provide an exact minimizer general algorithm, termed PUMF (Phase Unwrapping Max-Flow), considering convex pairwise pixel interaction potentials; namely we solve exactly all the phase unwrapping classical minimum  $L^p$  norm problems for  $p \geq 1$ . A set of experimental results illustrates the effectiveness of the proposed algorithm, and its competitiveness with state-of-the-art algorithms.

*Key Words: Phase unwrapping, interferometric synthetic aperture radar (InSAR), integer optimization, graph cuts, image processing, remote sensing.*

## Resumo

A Interferometria de Radar de Abertura Sintética (InSAR) é uma técnica de detecção remota cujo principal objectivo é medir a altitude do terreno. A capacidade de operar independentemente da hora do dia ou noite, bem como das condições climáticas, potenciou o uso de modelos digitais do terreno (MDT) obtidos via InSAR.

As técnicas de Desenrolamento de Fase visam, dada uma imagem de fase módulo- $2\pi$ , inferir a correspondente imagem de fase absoluta. Tal procedimento, sendo um passo crítico na cadeia de processamento em InSAR, constitui também, reconhecidamente, um dos seus problemas mais difíceis; este facto faz do Desenrolamento de Fase um problema crucial na produção de MDT baseados em InSAR.

Esta tese introduz uma nova abordagem a este problema, seguindo um paradigma de minimização de energia e utilizando técnicas de optimização com grafos. É proposto um algoritmo de minimização exacta, o PUMF (Phase Unwrapping Max-Flow), admitindo quaisquer potenciais de interacção convexos entre pares de píxeis. O PUMF resolve de forma exacta todos os problemas de desenrolamento de fase de mínima norma  $L^p$  com  $p \geq 1$ . Um conjunto de resultados experimentais ilustra a eficácia do algoritmo proposto, bem como o seu desempenho competitivo relativamente aos melhores algoritmos em Desenrolamento de Fase.

*Palavras chave: Desenrolamento de Fase, Interferometria de Radar de Abertura Sintética (InSAR), Optimização Inteira, Cortes em Grafos, Processamento de Imagem, Detecção Remota.*

## Acknowledgements

First and foremost I would like to thank my thesis supervisor, Prof. José Bioucas-Dias, for his generous, devoted and challenging guidance, his scientific creativity, and commitment to excellence. Thanks also to Prof. João Matos and all the núcleo 7 team. I also would like to thank the support of many friends, namely: Vasco, Filipa, Nunos, Pedro, Padre João, Fечи, João, Carlas, Jorge, Inês, Paulo and Isabel. Finally, last but not the least, thanks to all my family.

# Contents

<b>1</b>	<b>Introduction</b>	<b>1</b>
1.1	Proposed Approach . . . . .	2
1.2	Thesis Contextual Setting . . . . .	3
1.3	Dissertation Outline . . . . .	3
<b>2</b>	<b>Background: SAR Interferometry and Phase Unwrapping</b>	<b>4</b>
2.1	SAR Interferometry . . . . .	4
2.1.1	SAR Concept . . . . .	4
2.1.2	InSAR: Milestones, Concepts and Applications . . . . .	6
2.1.3	InSAR Geometry . . . . .	11
2.1.4	Decorrelation and Quality Maps . . . . .	14
2.2	Phase Unwrapping . . . . .	16
2.2.1	What is Phase Unwrapping? . . . . .	16
2.2.2	The Itoh Condition . . . . .	17
<b>3</b>	<b>Main Phase Unwrapping Approaches and State-Of-The-Art Algorithms</b>	<b>20</b>
3.1	Path Following Methods . . . . .	20
3.1.1	Residues . . . . .	21
3.1.2	Branch Cuts Algorithms . . . . .	22
3.1.3	Quality Guided Algorithms . . . . .	24
3.2	Minimum Norm Methods . . . . .	24
3.2.1	The Minimum $L^p$ Norm . . . . .	25

3.2.2	$L^2$ Norm Algorithms . . . . .	26
3.2.3	$L^1$ Norm Algorithms . . . . .	27
3.2.4	Low $p$ Valued $L^p$ Norm Algorithms . . . . .	28
3.3	Bayesian and Parametric Methods . . . . .	28
<b>4</b>	<b>The PUMF Approach</b>	<b>30</b>
4.1	Problem Formulation . . . . .	30
4.2	Energy Minimization by a Sequence of Binary Optimizations . . . . .	32
4.2.1	An Existence Theorem for Energy Minimization . . . . .	32
4.2.2	Mapping Binary Optimizations onto Graph Max-Flows . . . . .	33
4.2.3	Energy Minimization Algorithm . . . . .	37
4.2.4	Clique Potentials . . . . .	38
<b>5</b>	<b>PUMF Performance</b>	<b>41</b>
5.1	Gaussian Hills . . . . .	41
5.2	Shear Ramps . . . . .	42
5.3	Long's Peak . . . . .	46
5.4	Benchmarking . . . . .	48
<b>6</b>	<b>Concluding Remarks</b>	<b>52</b>
<b>A</b>	<b>Proof of Theorem 1</b>	<b>53</b>

# List of Figures

2.1	Radar resolution . . . . .	6
2.2	The synthetic aperture radar (SAR) principle . . . . .	7
2.3	InSAR: XTI configuration . . . . .	8
2.4	Differential InSAR: subsidence in Las Vegas . . . . .	10
2.5	PSInSAR: subsidence in Lisbon suburbs . . . . .	11
2.6	Current flow obtained with SRTM-ATI mode: Dutch Wadden Sea . . . . .	12
2.7	InSAR geometry in a flat earth . . . . .	13
2.8	Phase unwrapping problem ill posedness . . . . .	17
3.1	Integration path independence . . . . .	21
3.2	Residues and composition of elementary loops . . . . .	22
3.3	Branch cuts configuration . . . . .	23
4.1	A site and first order neighbours . . . . .	31
4.2	Graphs structure . . . . .	36
4.3	A classical $L^p$ norm as a quantized potential . . . . .	40
5.1	Gaussian surface application example . . . . .	43
5.2	PUMF complexity experimental estimates vs. reference bound . . . . .	44
5.3	Gaussian surface with a quarter null application example . . . . .	45
5.4	Shear planes surface application example . . . . .	47
5.5	Long's Peak surface application example . . . . .	49

# List of Tables

5.1	PUMF vs. reference PU algorithms. Phase unwrapping problems presented in section 5.1 . . . . .	50
5.2	PUMF vs. reference PU algorithms. Phase unwrapping problems presented in section 5.2 . . . . .	50
5.3	PUMF vs. reference PU algorithms. Phase unwrapping problem presented in section 5.3 . . . . .	50

# Chapter 1

## Introduction

This thesis presents a new *energy minimization* framework to phase unwrapping and illustrates its relevance to interferometric synthetic aperture radar (InSAR) applications.

InSAR imaging comprises an ensemble of techniques that provide measurements on surface topography and surface deformation. Other characteristics, such as land classification or motion tracking, can also be obtained using InSAR. Capable of day and night, in all weather, measurements, with an ever improving spatial resolution due to developments in sensors and processing algorithms, InSAR is an increasingly popular remote sensing technique [1], [2].

SAR interferometry<sup>1</sup> utilizes two or more complex-valued images of the same scene to infer the desired information. Those images must differ by a certain feature, like a slight difference in the sensor flight track, difference in the acquisition time, or difference in the used wavelengths. In spite of a possible resemblance with optical stereoscopy, SAR interferometry works with pixel-to-pixel phase differences between the images, instead of intensity (i.e., amplitude) values; this is a crucial distinction that calls for different processing techniques, as well as a complementary set of applications [1].

Like several other imaging technologies, where the information lies in the phase rather than amplitude, in SAR interferometry phase can be observed only in the principal interval  $]-\pi, \pi]^2$ , i.e., the acquisition system wraps the phase around that interval. A necessary

---

<sup>1</sup>*Interferometric synthetic aperture radar* (InSAR) and *SAR interferometry* are two terms used interchangeably throughout the text. SAR is the acronym for Synthetic Aperture Radar.

<sup>2</sup>In radians.

operation is, therefore, the removing of the  $2\pi$ -multiple ambiguity in order to recover the true (i.e., *absolute*) phase from the *wrapped* phase: the *phase unwrapping* (PU) problem.

Although there is a quite extensive published literature, phase unwrapping cannot be considered a mature field, but instead, an active research topic [3]. To deal with absolute phase discontinuities and noise, is still an open question to which lots of ongoing research efforts are being devoted. In radar interferometry, these discontinuities are a result of well known identified situations, namely, steep slopes on the ground or typified bad SAR geometries inducing, for instance, shadowing and layover [4]; noise, due to multiple sources, is also an ubiquitous origin of phase discontinuities. Improvement on algorithms accuracy, robustness, and speed is the aim of phase unwrapping research.

Being a critical step in the InSAR processing chain, phase unwrapping is also considered to be one of the most challenging problems for InSAR successful application [5]. With an ongoing wide research and operational set of InSAR applications, e.g., generation of digital elevation models, measurements of glaciers flows, and mapping of earth quakes, volcanoes and subsidence phenomena, phase unwrapping is a worthwhile problem to be addressed in the geographical information science communities [1].

## 1.1 Proposed Approach

The framework herein presented considers phase unwrapping as an optimization problem. For each pixel a certain  $2\pi$  multiple is to be found, such that when added to the wrapped phase, it renders, tentatively, the absolute phase. This *estimation* is achieved through the minimization of a so-called *energy* function, using a sequence of binary optimizations, inspired by the  $\mathbb{Z}\pi$ M algorithm [6]. Each of these binary optimizations is solved via a max-flow/min-cut formulation, using recent results on binary energy minimization [7]. Accordingly, the algorithm is termed PUMF, for Phase Unwrapping Max-Flow.

PUMF competes with state-of-the-art PU algorithms, in a series of shown benchmarking representative problems. We exemplify its effectiveness by presenting applications comprising hard artificial problems and synthesized InSAR data.

## 1.2 Thesis Contextual Setting

The main ideas underlying PUMF are due to my advisor, José Bioucas-Dias; in fact, this thesis benefited from more than a decade long of research activity on phase unwrapping at the Communications Theory and Pattern Recognition Group of the Instituto de Telecomunicações at Instituto Superior Técnico, Portugal. In this context, the thesis aims at helping to bridge the gap between geographical information systems and InSAR research areas.

## 1.3 Dissertation Outline

Chapter 2 gives a basic background on radar interferometry and phase unwrapping, followed by a quick review of the main phase unwrapping approaches and state-of-the-art algorithms, in Chapter 3. Then, Chapter 4 presents the PUMF approach, with emphasis on its theoretical support and on algorithm aspects, as well. Chapter 5 presents the experimental results obtained with PUMF, as well as benchmarks against reference algorithms. Finally, Chapter 6 draws conclusions from the work done, setting directions for future work.

## Chapter 2

# Background: SAR Interferometry and Phase Unwrapping

In this chapter, we set the stage by giving some background on SAR interferometry and on phase unwrapping. Without entering into the technicalities of SAR processing, we browse through some of the main interferometry topics, and we emphasize the critical importance of phase unwrapping for the generation of InSAR products. Next, we give a brief overview of the phase unwrapping problem.

### 2.1 SAR Interferometry

#### 2.1.1 SAR Concept

Remote sensing systems can be classified as either active or passive, according to whether they provide their own energy source for illumination or not [8]. Most of the active type systems are radar based<sup>1</sup> systems [9], [4]. Radar operates at the microwave range of frequencies (wavelengths between 1cm and 1m), which propagate through clouds, rain, and fog practically without disturbance. Radar systems allow, thus, a 24 hours a day and nearly all-weather operation [4].

Radar imaging spatial resolution is illustrated in Fig. 2.1 (a), which shows a radar platform at velocity  $V$  illuminating the ground in a resolution cell having a *ground range*

---

<sup>1</sup>Radar is the acronym for RAdio Detection And Ranging.

dimension  $\Delta X$  and an *azimuthal* dimension  $\Delta Y$ . In that sketch the sensor goes on, transmitting radar pulses and retrieving their echoes, using a side looking geometry. Still referring to Fig. 2.1 (a), range  $r$  (slant range in SAR jargon) is defined as the distance from the antenna to the target and ground range  $x$  as its projection on the ground.

Range resolution can be defined as the shortest range distance,  $\Delta r$ , for which two point targets produce non-overlapping echoes. As illustrated in Fig. 2.1 (b), a pulse with duration  $\tau$  gives, therefore, a range resolution  $\Delta r = \frac{c\tau}{2}$ , where  $c$  is the speed of light. Fine range resolutions require, then, short pulses, which brings both a technological and an economical problem. To overcome this, there exist signal processing techniques, namely, *chirp pulse compression* which consists in transmitting long pulses (chirps), and then compressing the echoes[10]. The ground range resolution is approximately given by  $\Delta X \approx \frac{c/2}{B} \frac{1}{\sin(\theta)}$ , where  $c$  stands for light velocity,  $B$  for the chirp frequencies bandwidth, and  $\theta$  for the *look angle* [see Fig. 2.1 (a)]. The  $\sin(\theta)$  term accounts for the projection of the range resolution on the ground [10], [4, Chap. 1], [11].

Concerning azimuthal resolution, it is a matter of how much the antenna is capable of focusing the received and transmitted microwaves into a sharp beam. It is well known, from antenna theory, that this depends on the antenna size or aperture<sup>2</sup> [12]. Namely, we have  $\Delta Y \approx \frac{\lambda}{D}r$ , where  $\lambda$  stands for wavelength,  $D$  for the antenna aperture, and  $r$  for range [4, Chap. 1], [11]. This expression for  $\Delta Y$  tells us that, given the wavelength and the range distance, we can get finer resolutions by increasing the antenna size. Considering, e.g., a desired azimuthal resolution of 10 m, and a typical range distance of 800 km (approximately the ERS-1/2 satellites range distances) for a *C-band* ( $\lambda = 5.6$  cm) radar, we must have an aperture  $D = 448$  m, which is obviously a prohibitive antenna size to put on-board any existing satellite.

The synthetic aperture technique was developed to overcome the antenna size limitation on resolution. Commonly attributed to Carl Wiley (Goodyear Aircraft Corporation, 1951), its principle consists on letting the radar antenna fly over the length of the desired aperture, collecting data, and later processing it as if it was obtained from a physically large antenna (see Fig. 2.2). These signal processing algorithms thus *synthesize* an aperture. SAR boosted the development of radar imaging applications, first military and then

---

<sup>2</sup>These two concepts are not rigorously equivalent but very similar in practice.

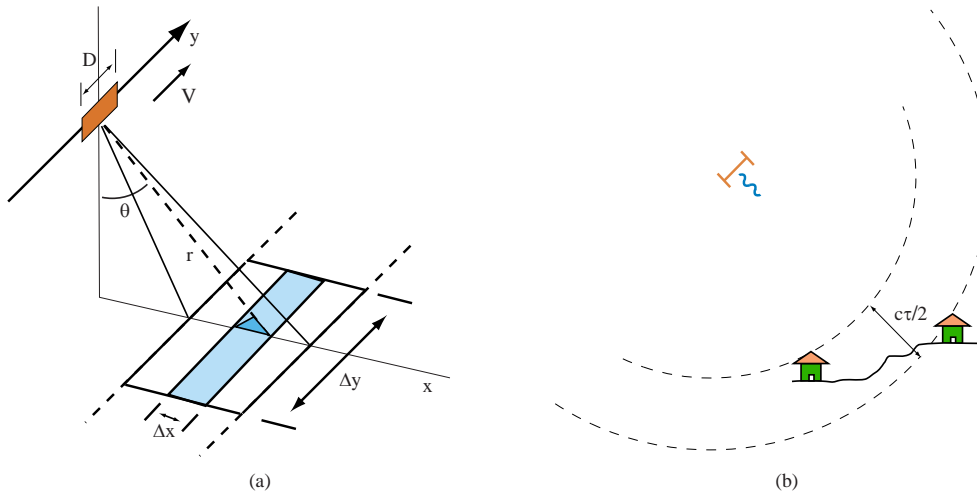


Figure 2.1: (a) Radar spatial resolution cell. (b) Range resolution.

civilian. As an example, the TerraSAR-X satellite scheduled to be launched in 2006, will provide SAR images of up to 1 m resolution [13].

### 2.1.2 InSAR: Milestones, Concepts and Applications

In this section and in part of the next one, we follow very closely the InSAR review papers by Bamler *et al.* [2], and Rosen *et al.* [1].

Interferometric SAR evolved both from the development of SAR and of interferometric techniques used in radio astronomy. The very first reported application of radar interferometry was made by Rogers and Ingalls [14], in a work on the mapping of the surface reflectivity of Venus, in 1969. In 1972, Zisk published a work on measurements of the moon topography [15], and two years later Graham first reported the first application of InSAR to Earth observation [16]. Therein, he employed an airborne system with an ensemble of two SAR antennas constituting a *cross-track interferometer*, with which he obtained the first InSAR measurements of Earth topography. The collected data over Puerto Rico served as proof-of-concept generation of topography mapping using InSAR.

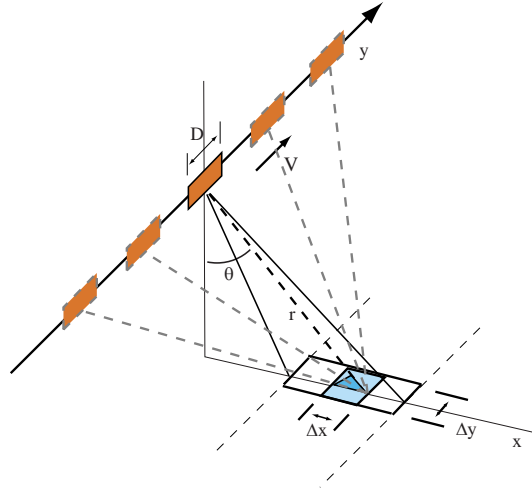


Figure 2.2: The synthetic aperture radar (SAR) principle.

### Cross-track interferometry

**DEM Generation** Figure 2.3 sketches a typical InSAR *cross-track interferometry* (XTI) configuration. In this mode, two or more SAR antennas separated by a certain cross-track<sup>3</sup> baseline distance acquire images over the same area via slightly different directions. As shown below, in Section 2.1.3, given the two ranges  $r_1$  and  $r_2$  and the two SAR antennas locations, it is possible to recover, by triangulation, the 3-D position for each ground resolution cell, and thus produce a digital elevation model (DEM). Unlike classical stereo techniques, which involve the selection of *sparse* homologous points in the image pairs and for which image contrast is needed, InSAR works by measuring phase differences on *every* pixel. This can be so, because as SAR is a coherent system [17], it is possible to retrieve the phase of the electromagnetic radar waves arriving at the sensors and, thus, produce phase images. This fact additionally brings automation to the processes of registration of the SAR images entering into the interferometric measurement, the retrieval of the interferometric phase difference, and conversion of the results into digital elevation models (DEM) of the terrain [1], which constitutes a benefit of the InSAR framework.

The most prominent application of spaceborne cross-track interferometry was made by the Shuttle Radar Topography Mission<sup>4</sup> (SRTM) in 2000. The Endeavour shuttle (NASA)

<sup>3</sup>We call baseline to the vector joining two platforms. A cross-track baseline, by definition, has a non null projection in the plane perpendicular to the flight tracks or orbits.

<sup>4</sup>A joint mission of NASA (National Aeronautics & Space Administration), DLR (German Aerospace

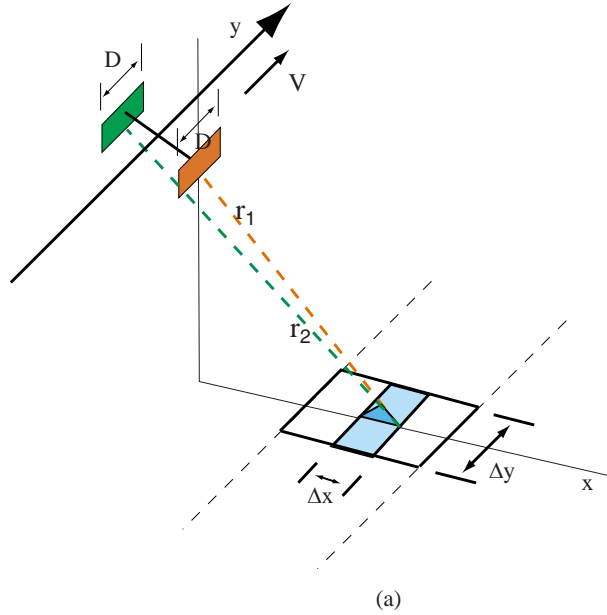


Figure 2.3: InSAR: XTI configuration.

was equipped with a main antenna mounted on the cargo bay, and an outboard antenna at the end of a 60 *m* mast. In 10 days it covered the Earth surface between latitudes 60° North and 54° South. The global DEM produced, 30 *m* spatial sampling, complies with DTED2<sup>5</sup> specifications which, namely, call for 16 *m* (90%) absolute vertical height accuracy, and 20 *m* (90%) absolute horizontal circular accuracy<sup>6</sup>.

**Motion Mapping - Differential Interferometry** Besides the SRTM mission, interferometry with SAR satellites has been, to date, made on a *repeat-pass* basis, which means that the acquisition of the image pair (or multiple) is not simultaneous, but made in successive times of revisit to the ground spots at issue. During those time lags (e.g., the ERS satellite revisit time is 35 days) propagation properties, as well as surface, may change. A ground motion  $\Delta r$  in the range direction translates into a differential phase shift of

$$\phi_{diff} = 2 \times \frac{2\pi}{\lambda} \Delta r, \quad (2.1)$$

Center), and ASI (Italian Spatial Agency).

<sup>5</sup>Digital Terrain Elevation Data level 2 specifications (<http://www.nga.mil/ast/fm/acq/89020B.pdf>).

<sup>6</sup>For accuracy definitions see, e.g., [18].

where the factor 2 accounts for the two-way round trip of the radar pulse. However, a measured differential phase shift may include, as well, the atmospheric contributions due to change in propagation properties. The most employed technique to suppress those unwanted contributions, relies on producing several independent *interferograms* (the images containing the phase shifts) and then to average them. This average filter can be applied assuming that atmospheric properties evolve in an approximately random fashion. Knowing  $\Delta r$  and acquisition times, it is possible to infer the surface velocity (in the range direction). Other changes in the ground point scattering properties, and noise, may also contribute to temporal decorrelation; however, in many cases *cm*-accuracy is achievable for  $\Delta r$  measurements.

It should be noted that in practice, whether for spaceborne or airborne systems, the platform does not repeat exactly the same path and, thus, introduces a non-zero cross-track baseline. This brings in an ambiguity of motion versus topographic induced phases that can be resolved, if either an accurate DEM or a set of different baseline interferograms are available [19]. This ambiguity suppression must assume a certain kinematic model for the ground motion [19].

Figure 2.4 shows a mapping of subsidence<sup>7</sup> in Las Vegas (Nv, USA), between 1992 and 1997, using differential interferometry from ERS images [20].

**Motion Mapping - Persistent Scatterers Interferometry** Time changes of propagation and surface properties tend to produce a decorrelation between the images acquired at different times. Although this temporal decorrelation sets limits on the time spanned between image acquisitions, to allow the production of meaningful interferograms, it has been observed that some sparse ground scatterers present an outstanding time persistent correlation. Persistent (or permanent) scatterers interferometry (PSInSAR) is a differential interferometry technique that makes use of this fact, to reach extremely accurate displacement measurements, being able to produce maps of subsidence/uplift rates to an accuracy of less than 1 mm/year. For that, a large number of phase images (30 – 100) is required, ranging a period that is usually between 5 and 12 years. For each of these persistent scatterers, PSInSAR algorithms can produce an individual displacement history

---

<sup>7</sup>Ground down lift.

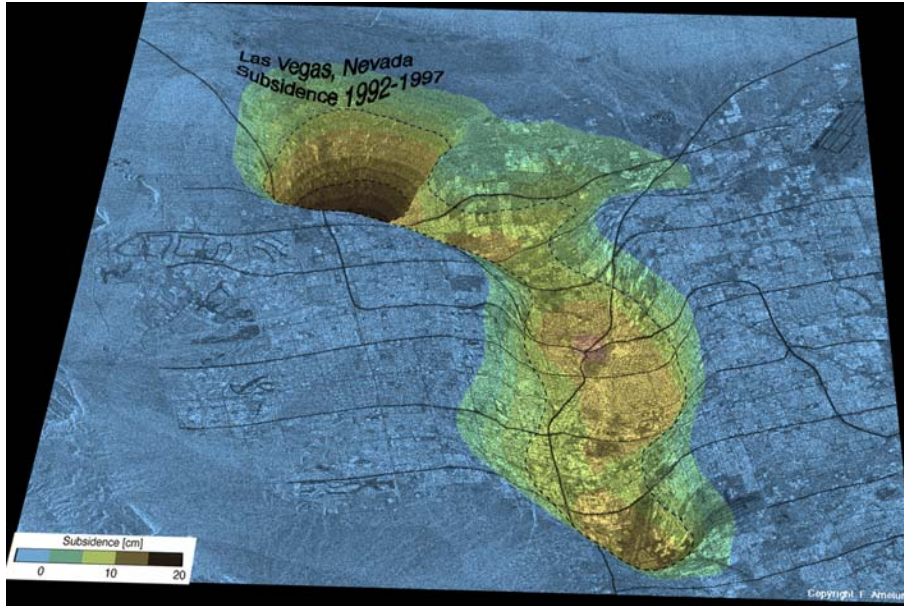


Figure 2.4: Differential InSAR derived subsidence in Las Vegas between 1992 and 1997. Taken from [20].

sampled at each image acquisition epoch.

The major limitation of PSInSAR is the inhomogeneity of the persistent scatterers spatial distribution, which gives predominance to urban man-made features, or natural rocky areas.

Figure 2.5 shows a segment of an amplitude radar image covering an area along the Tagus river near Lisboa, Portugal. Detected persistent scatterers are overlaid and represented by coloured dots that correspond to different subsidence rates; red means high subsidence rates (around  $-12\text{mm/year}$ ). These results were obtained in the framework of the ESA/UE TerraFirma project.

### Along-track interferometry

Some configurations employ two radar antennas displaced in the along-track direction, following each other at a short distance, and usually mounted on the same platform. Time delay between the two acquisitions is very often in the range  $10 - 100\text{ ms}$ , and in practice the two antennas acquire images from the same position, such that phase topographic signature is null. This so-called *along-track interferometry* (ATI) allows the measurement

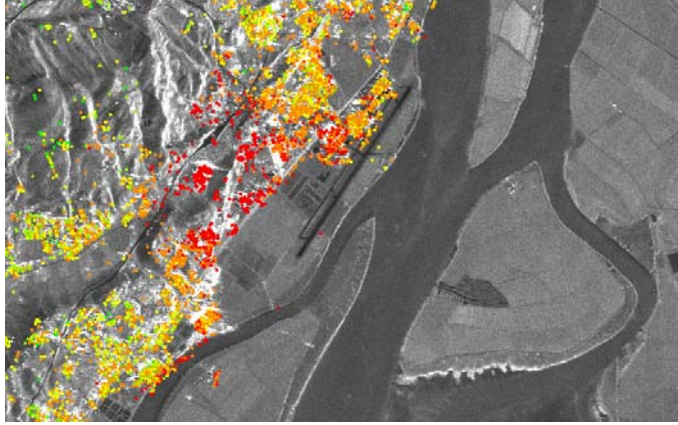


Figure 2.5: Persistent scatterers near Lisbon, Portugal (data processed by TRE in the framework of the ESA/EU Terrafirma project).

of fast surface displacements of the range of m/s, with rapid decorrelation properties.

Mostly used in airborne systems, SRTM remains one of the few spaceborne experiments with ATI. In [21] the authors used the SRTM-ATI time lag of about 0.5 ms between the acquisition pairs, to produce measurements on the currents of the Dutch Wadden Sea (Fig.2.6).

### 2.1.3 InSAR Geometry

Digital elevation models generation is virtually the primal application of InSAR, whether by defining a core concept in most InSAR applications, whether by being historically the first operational product. In this section, we briefly browse the basics of the geometry of the correspondent cross-track InSAR mode.

Let us use labels 1,2 to identify two SAR sensors forming an interferometer<sup>8</sup>. The phase  $\phi^{1,2}$  arriving at a pixel on each sensor has the following contributions:

$$\phi^{1,2} = \underbrace{\frac{2\pi}{\lambda} 2r^{1,2}}_{\phi_r^{1,2}} + \phi_{scat}^{1,2} + \phi_{prop}^{1,2} + \phi_{noise}^{1,2}, \quad (2.2)$$

where  $\phi_r$  is the phase due to the round trip propagation distance,  $\lambda$  is the used wavelength (thus,  $\frac{2\pi}{\lambda}$  is the wave number),  $2r$  represents the round trip range distance (from the sensor to the ground and back again),  $\phi_{scat}$  stands for the change in phase due to ground

---

<sup>8</sup>Whether of the single-pass or repeat-pass type.

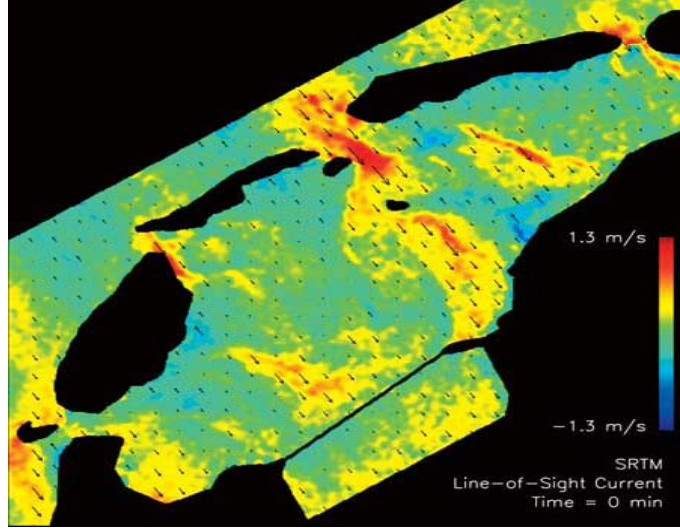


Figure 2.6: Range direction current flow obtained by SRTM-ATI acquisition over the Dutch Wadden Sea. Taken from [21].

scattering,  $\phi_{prop}$  stands for atmospheric propagation delay<sup>9</sup>, and  $\phi_{noise}$  stands for a phase shift due to noise<sup>10</sup>.

Neglecting time, spatial and geometrical decorrelation, we may assume that  $\phi_{prop}^2 = \phi_{prop}^1$ , and  $\phi_{scat}^2 = \phi_{scat}^1$ . So, also neglecting noise, it comes for the phase difference

$$\phi = \phi^2 - \phi^1 = \phi_r^2 - \phi_r^1 = \frac{4\pi}{\lambda} \Delta r, \quad (2.3)$$

where  $\Delta r = r^2 - r^1$ . We will refer in more detail to decorrelation and noise issues, in the next section.

Let us now consider a general interferometric configuration as depicted in Fig. 2.7<sup>11</sup>, in which, for simplicity, we consider a flat earth. Sensor 1 and sensor 2 are, respectively, at range distances  $r^1$  and  $r^2$  from a resolution cell in the ground, which is at a height  $a$  from a reference level.  $B$  is the baseline distance between the two sensors, with  $B_{\perp}$  and  $B_{\parallel}$  being its perpendicular and parallel components respectively. Range distances  $r^1$  and  $r^2$  are much larger than  $B$ , so we have:

<sup>9</sup>The main influence is due to water vapour in the troposphere.

<sup>10</sup>Noise may have several sources, namely, thermal noise.

<sup>11</sup>Sketch taken from [22].

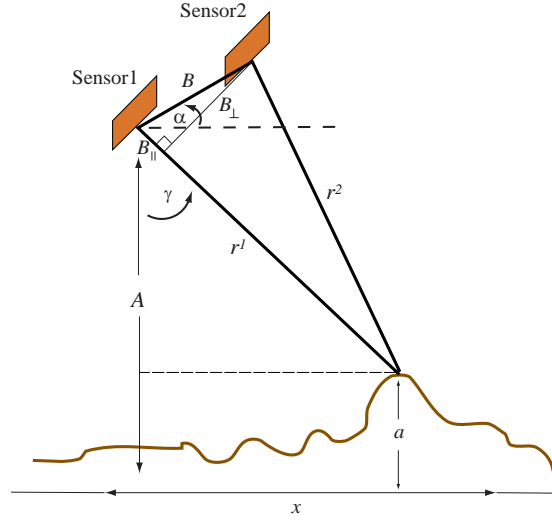


Figure 2.7: InSAR geometry in a flat earth. Taken from [22].

$$r^2 - r^1 \approx B_{\parallel} \quad (2.4)$$

$$= B \cos\left(\frac{\pi}{2} - \gamma + \alpha\right) \quad (2.5)$$

$$= B \sin(\gamma - \alpha). \quad (2.6)$$

We are actually interested in obtaining the ground resolution cell height  $a$ . From Fig. 2.7 we have:

$$a = A - r^1 \cos(\gamma), \quad (2.7)$$

and from (2.6)

$$\gamma = \arcsin\left(\frac{r^2 - r^1}{B}\right) + \alpha, \quad (2.8)$$

so, inserting (2.8) into (2.7) we get

$$a = A - r^1 \cos\left[\arcsin\left(\frac{r^2 - r^1}{B}\right) + \alpha\right]. \quad (2.9)$$

Finally, from (2.3) and noting that  $\Delta r = r^2 - r^1$ , we get

$$a = A - r^1 \cos \left[ \arcsin \left( \frac{\phi \lambda}{4\pi B} \right) + \alpha \right]. \quad (2.10)$$

Expression (2.10) is a fundamental one, as it gives the ground cell height  $a$  from the interferometric phase  $\phi$ , and via the acquisition geometry parameters  $A, r^1, B$  and  $\alpha$ . Computing the associated ground range  $x = \sqrt{(r^1)^2 - (A - a)^2}$ , we are then able to produce a digital elevation model.

#### 2.1.4 Decorrelation and Quality Maps

Unlike most imagery, SAR image pixels are complex-valued. In fact, a complex number is the natural representation of both the amplitude and the phase retrieved at each SAR sensor cell.

A common model for the value of a certain pixel in the  $i^{th}$  image entering into an interferogram is given by, [6], [22, Chap.2]:

$$z_i = A_i e^{j\phi_i} + \eta_i, \quad (2.11)$$

where  $A_i = A e^{j\psi_i}$  is a random variable accounting for a complex amplitude, resulting from the complex sum of the echoes backscattered from the various scatterers in the same resolution cell,<sup>12</sup>  $\phi_i$  accounts for the round trip propagation for the pulse backscattered at this cell, and  $\eta_i$  is a random variable accounting for electronic noise [6], [22, Chap.2]. Furthermore, considering that the ground surface is rough (comparing to the wavelength), that on each resolution cell the scatterers are randomly spatially distributed, and that none of the scatterers is predominant, then,  $A_i$  is a zero mean circular gaussian random variable [23], [22]. For any two homologous pixels in images 1, 2, we have  $E(A_1 A_2^*) = \rho \sqrt{E(|z_1|^2) E(|z_2^*|^2)} = \rho \theta^2$ , where  $\theta$  is the (common) standard deviation of random variables  $A_1, A_2$  and  $\rho$  is their correlation coefficient<sup>13</sup>.

It is trivial to show that, if the random variables  $A_1$  and  $A_2$  are totally correlated ( $\rho = 1$ ) and if noise is neglected, then the round trip phase difference  $\phi = \phi_2 - \phi_1$  between

---

<sup>12</sup>On each ground resolution cell, there are a certain number of elementary scatterers, each of which is located at a different distance from the sensor (besides possessing diverse scattering properties); the sensor resolution cell “sees” the complex sum—the so-called coherent sum— of all these contributions.

<sup>13</sup>As usual, E stands for the expected value operator.

the two images can be given by

$$\phi = \arg(z_2 z_1^*), \quad (2.12)$$

where  $\arg(z) \equiv \arctan \left[ \frac{\text{Im}(z)}{\text{Re}(z)} \right]$ ;  $\phi$  is the so-called *interferometric phase*, which we will simply refer to as phase, whenever that is not misleading;  $z_2 z_1^*$  is usually referred to as the *interferogram*. However, besides noise, there are in practice other decorrelation sources, from which we emphasize:

- Spatial decorrelation: results from misregistration between the images entering into the interferogram. This is, in practice, a delicate issue, as if the SAR system has a narrow enough impulsive response, then it can be sensible even to misregistration at the subpixel level.
- Geometric decorrelation: results from variations in phase of targets inside a resolution cell due to different incidence angles.
- Temporal decorrelation: results from time dependent phase fluctuations due to ground motion, ground scattering properties, or propagation conditions.

Thus, in the presence of decorrelation and noise, expression (2.12) is useless and some kind of statistical inference is used instead. A commonly used one is through the maximum-likelihood estimator, which can be shown [24], [25] to be given by

$$\hat{\phi} = \arctan \left[ \frac{\text{Im}(\sum_k z_1 z_2^*)}{\text{Re}(\sum_k z_1 z_2^*)} \right], \quad (2.13)$$

where  $\sum_k$  extends over a window with  $k$  pixels, over the images, where  $\phi$  is assumed to be constant.

A last note about the so-called *quality maps* is worthy. These maps are ancillary images that give information on the quality of the retrieved interferometric phase  $\phi$ . The usually preferred criterion to measure quality is the absolute value of the correlation coefficient, the so-called coherence:

$$\alpha = |\rho| = \left| \frac{\text{E}(z_1 z_2^*)}{\sqrt{\text{E}(|z_1|^2) \text{E}(|z_2^*|^2)}} \right|. \quad (2.14)$$

Generally, coherence is low for pixels having high decorrelation or original phase discontinuities. When available, quality maps carry very useful information to some of the existing

*phase unwrapping* processing algorithms. We will cover the basics of *phase unwrapping* in the following section.

## 2.2 Phase Unwrapping

### 2.2.1 What is Phase Unwrapping?

We have shown above that phase holds the requested InSAR information on ground height. After acquiring two SAR images  $S_1$  and  $S_2$ , and producing the correspondent interferogram  $I = S_1 S_2^*$ , the interferometric phase can finally be obtained according to expression (2.12). This procedure encloses, however, an ambiguity that is intrinsic to the SAR phase acquisition systems [10]. Instead of the absolute (i.e, the true) phase, only its principal value, which is defined as the remainder of phase after the subtraction of the maximum  $2\pi$ -multiple that is less or equal than the phase value, plus a further subtraction of a  $\pi$  quantity, can be detected and stored. Correspondingly the principal interval, which is the set of all possible principal values, is  $]-\pi, \pi]$ <sup>14</sup>. Accordingly, the ambiguity is also present in the interferometric phase given by (2.12)<sup>15</sup>. In mathematical terms, the principal value of the phase is also known as, basically, its *modulo-2 $\pi$*  value, which can be seen as the outcome of wrapping the phase around a  $2\pi$  length interval ( $2\pi$  radians corresponds to a full wavelength cycle), resulting in the so-called *wrapped phase*. *Phase unwrapping* (PU) is the inverse process: the recovery of the absolute phase from the wrapped phase. Its goal is, then, to remove the  $2\pi$ -multiple ambiguity.

Phase unwrapping is an ill-posed problem [26], if no further information is added. In fact, given any wrapped phase image, there is an infinite number of possible corresponding unwrapped phase images<sup>16</sup>. This lack of uniqueness for the unwrapping of an image *per se*, is illustrated in Fig. 2.8 with a toy example using  $3 \times 3$  size images with pixels values in principal interval units. In Fig. 2.8 (a) a modulo- $2\pi$  wrapped image is shown, together with a corresponding mesh rendering. Figures 2.8 (b) and 2.8 (c) present two different possible

<sup>14</sup>Without loss of generality any  $2\pi$ -length interval could have been defined as the principal interval.

<sup>15</sup>It could, in principle, be argued that, even so, the (absolute) interferometric phase could fall within the principal value, in which case there would be no ambiguity. Nevertheless, the travel path difference between the two sensors always amounts, at least, to some tens of meters, and according to (2.3) the interferometric phase magnitude, then, far exceeds the  $2\pi$  value.

<sup>16</sup>In other words, given any image, there is an infinite number of images that are  $2\pi$ -congruent with it.

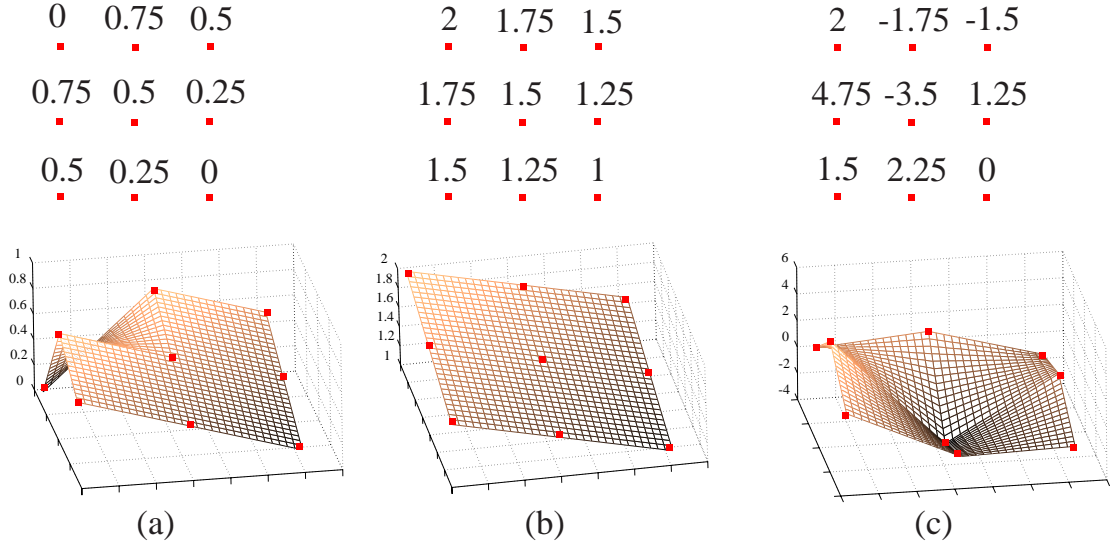


Figure 2.8: (a) Modulo- $2\pi$  wrapped image and its mesh rendering. (b) Possible unwrapped solution and its mesh rendering. (c) A second possible unwrapped solution and its mesh rendering. All the values are in principal interval units.

corresponding unwrapped images, along with their mesh renderings which emphasize how different those solutions are.

## 2.2.2 The Itoh Condition

### The Itoh Method

An assumption taken by most phase unwrapping strategies, is that the absolute value of phase differences between neighbouring pixels is less than  $\pi$ , the so-called Itoh condition [27]. If this assumption is not violated, it eliminates the ill-posedness of the problem, allowing the absolute phase image to be easily determined up to a constant. Introducing some simple notation, let us define the wrapper operator  $\mathcal{W}(\cdot)$  by

$$\begin{aligned} \mathcal{W} : \mathbb{R} &\longmapsto ] - \pi \pi] \\ \phi &\longmapsto \phi - 2\pi k, \end{aligned} \tag{2.15}$$

where  $k \in \mathbb{Z}$  is such that  $(\phi - 2\pi k) \in ] - \pi \pi]$ . The operator  $\mathcal{W}$ , thus, wraps any phase  $\phi$  into the principal interval  $] - \pi \pi]$ , which, as referred previously, is a zero centred,  $2\pi$  length interval, that is, in essence, the modulo- $2\pi$  operator, with no loss of generality by

subtracting  $\pi$  radians. Let us also consider a sequence  $\{\phi_n\}$  of neighbouring pixels values over an absolute phase image, and define a corresponding sequence of linear differences by

$$\Delta\phi_n = \phi_n - \phi_{n-1}. \quad (2.16)$$

Hereafter,  $\phi$  will be denoting an absolute (i.e., unwrapped) phase, and  $\psi$  a wrapped phase; the  $\Delta$  operator definition will hold, irrespective of phase being an absolute or a wrapped one.

The Itoh condition can be expressed as

$$|\Delta\phi_n| \leq \pi, \quad (2.17)$$

and from (2.16), it comes immediately

$$\sum_{n=1}^m \Delta\phi_n = \phi_m - \phi_0, \quad (2.18)$$

as the intermediate sequence values cancel out each other. Now, from (2.15) we have  $\mathcal{W}(\phi_n) = \phi_n - 2\pi k_n$  ( $k_n \in \mathbb{Z}$ ) and so,

$$\Delta\mathcal{W}(\phi_n) = \phi_n - \phi_{n-1} - 2\pi(k_n - k_{n-1}), \quad (2.19)$$

where  $k_n, k_{n-1} \in \mathbb{Z}$ . We can, thus, introducing (2.16), write

$$\underbrace{\mathcal{W}[\Delta\mathcal{W}(\phi_n)]}_a = \Delta\phi_n \underbrace{- 2\pi(k_n - k_{n-1}) - 2\pi k}_b, \quad (2.20)$$

where  $k_n, k_{n-1}, k \in \mathbb{Z}$ , and  $2\pi k$  is the proper  $2\pi$  multiple to bring  $a$  into the principal interval. From (2.17) and knowing that by definition  $|a| \leq \pi$ , we have necessarily  $b = 0$ , which allows us to write,

$$\mathcal{W}[\Delta\mathcal{W}(\phi_n)] = \Delta\phi_n. \quad (2.21)$$

Finally, introducing (2.21) into (2.18) we obtain:

$$\phi_m = \sum_{n=1}^m \mathcal{W}[\Delta\mathcal{W}(\phi_n)] + \phi_0, \quad (2.22)$$

which gives us a procedure for obtaining the unwrapped phase on any pixel,  $\phi_m$ , from the wrapped phase values along any path linking that pixel to another, for which the absolute phase value,  $\phi_0$ , is known: the Itoh method. By covering the image with a path, it allows us to unwrap an entire image up to a constant (the absolute phase value for one pixel in the image) given that the Itoh condition is satisfied.

### A Smoothness Assumption

Again referring to Fig. 2.8, the image in Fig. 2.8 (b) clearly verifies the Itoh condition, while image in Fig. 2.8 (c) does not. These two images claim very different absolute solutions, the first one showing the smoothness assumption that Itoh condition holds for the absolute images. This is, in fact, the case in many InSAR applications, where the ground topography is very often smooth or, at least, piecewise smooth (at the range of scales that InSAR deals with).

It is instructive to note that the Itoh condition can also be understood as a version of the Nyquist sampling theorem. Nyquist’s theorem states that a continuous, bandwidth-limited, signal<sup>17</sup> can be completely reconstructed from a sampling made, almost everywhere, at a frequency greater or equal than its higher frequency component  $w$  [28]. This means that, the “minimum” sampling must have a  $2w$  frequency, for which the samples present a phase difference less or equal than  $\pi$  radians, which is exactly the Itoh condition (2.17). Furthermore, as stated in Nyquist’s theorem, Itoh condition can be relaxed just to be satisfied *almost everywhere* in the image.

Itoh condition lies at the heart of most phase unwrapping techniques, hence the emphasis we have put on it in this section. In the following one, we will briefly review the main phase unwrapping approaches and representative state-of-the-art algorithms.

---

<sup>17</sup>A continuous function whose Fourier transform power spectrum is limited [28].

## Chapter 3

# Main Phase Unwrapping Approaches and State-Of-The-Art Algorithms

We have seen that Itoh condition immediately provides a phase unwrapping method, which, as explained in the previous chapter, employs a path following concept. Nevertheless, it is unrealistic to expect it to be applicable everywhere, as terrain topography can present a very rich geometry, and therefore induce phase *discontinuities*, i.e., neighbour pixels phase differences larger than  $\pi$  radians, which constitute violations to the Itoh condition. Moreover, decorrelation and noise also introduce phase discontinuities.

In this scenario, the phase unwrapping problem is rather more difficult and a great number of solving techniques (exact or approximate) have been proposed in the literature. In this chapter, we succinctly overview the main approaches and highlight some of the representative algorithms.

### 3.1 Path Following Methods

Path following methods directly apply the concept, introduced in the Itoh algorithm, of discrete phase integration along a path. Given a starting pixel, for which the absolute phase is known, Itoh method prescribes on how to compute the absolute phase on any

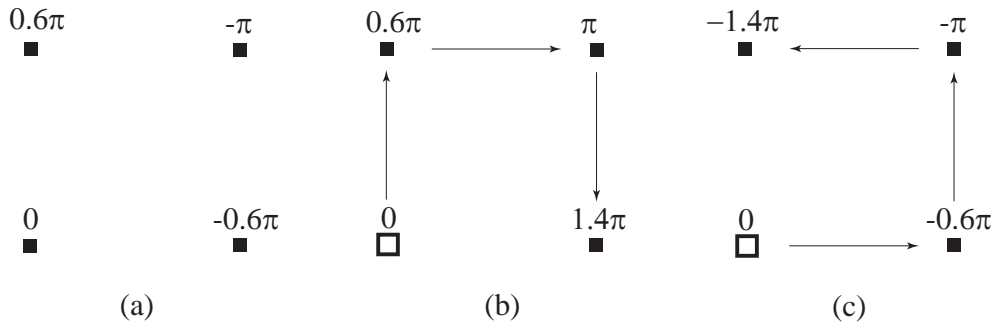


Figure 3.1: (a) Wrapped image. (b) A possible unwrapped solution. (c) Another possible unwrapped solution.

other pixel, without restricting the path linking the two whatsoever. A basic question arises, though, on whether this discrete integration is, in general, path independent. The answer to this question is negative, as is illustrated in Fig. 3.1, where a very simple counter-example is given. There, we depict an elementary wrapped image [Fig. 3.1 (a)] along with the unwrapped solutions obtained by employing the Itoh condition using two distinct paths linking the start pixel (represented by a hollow square) and the end pixel [Figs. 3.1 (b) and (c) respectively]. In what follows, we call *parallel paths* to any two (or more) paths sharing the same start and end pixels. As can be seen, in this case the integration is path dependent.

### 3.1.1 Residues

This path dependence phenomena in 2D phase unwrapping was first reported by Ghiglia et al. in [29]. There, furthermore, the authors observed that these inconsistencies were restricted to some regions on the phase image.

We note here that path integration dependence among two parallel<sup>1</sup> paths, can be tested by reverting the direction of one of them, and then integrating along the resultant closed loop path. Clearly, there is path dependence *if and only if* that quantity does not evaluate to zero.

Accordingly, to identify in full detail the inconsistencies locations in the image, Ghiglia et al. devised the (natural) strategy of path integrating the phase around every elementary  $2 \times 2$  loop; whenever that sum is not zero, it signals an inconsistency located precisely on

<sup>1</sup>By definition, path integration dependence is to be tested between parallel paths.

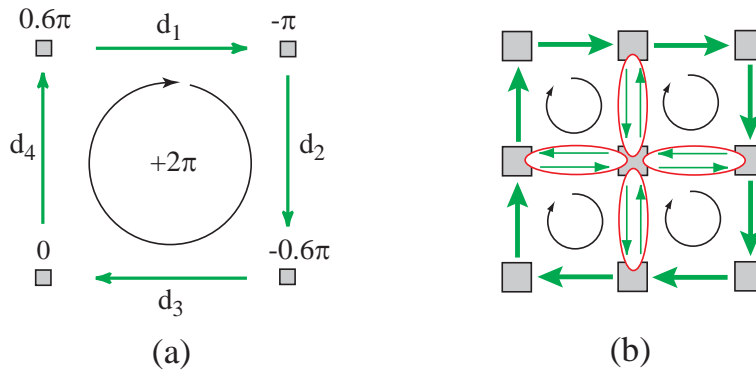


Figure 3.2: (a) An elementary closed loop having a residue. The path integration always sums up to a  $2\pi$  multiple, and in this case the residue charge is positive. (b) Any closed loop can be given as composition of elementary closed loops. In this sketch each pair of cancelling elementary path components is signalled by a red ellipse. The remaining components constitute the original outer closed path.

that loop. Later, the term *residue*<sup>2</sup>, instead of inconsistency, was introduced by Goldstein et al. in [30], and became the standard term ever since. By convention, residues are computed using counter-clockwise closed loops, the absolute value of the sum is always a  $2\pi$  multiple<sup>3</sup>, as illustrated in Fig. 3.2(a), and its signal defines the *residue charge* sometimes also termed *residue polarity*. It should be noted that a  $2 \times 2$  loop is elementary, in the sense that it is the shortest closed path that we may define and, accordingly, any closed path can be given by a composition of all such elementary loops that it encloses; Fig. 3.2(b) illustrates this. Therefore, given two parallel paths and considering again the correspondent closed loop, the sum of the enclosed residues is an effective criterion for inconsistency detection. We must remark at this point that, as above referred, while a residue implies a phase discontinuity existence, the converse implication does not hold. Therefore, additional information is very often, even if implicitly, introduced, as will become apparent in the next sections.

### 3.1.2 Branch Cuts Algorithms

A natural strategy to overcome path dependence in path following phase unwrapping methods, is to connect opposite charge residues with certain lines with which integration

<sup>2</sup>In a clear resemblance with complex analysis.

<sup>3</sup>It can be easily shown [31, Chap.2].

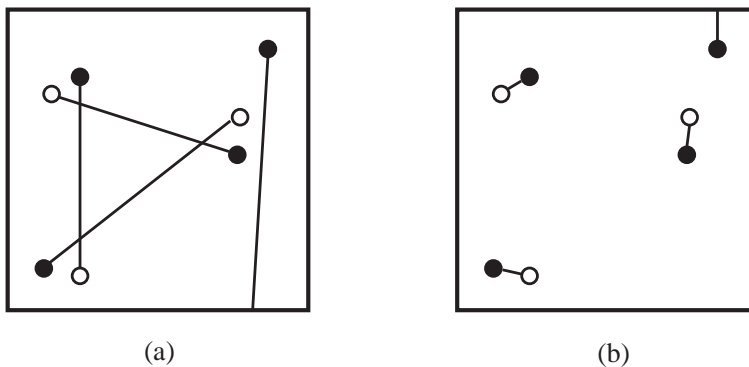


Figure 3.3: Example of residues and respective possible branch cuts configurations (Taken from [31]). Positive charged residues are represented by black dots and negative charged ones by white dots. (a) Ill branch cuts configuration. (b) Minimum length branch cuts configuration.

paths are not allowed to have cross-overs. In this way, the net charge of possible residues that may be enclosed on any path, is necessarily zero and, as argued in the previous section, there is no path dependence phenomena. Those lines are the so-called *branch cuts*<sup>4</sup>; other valid branch cuts are those linking a residue to a border of the image (it makes it impossible for any path to encircle the residue). From the many PU algorithms of the branch cuts type published in the literature, we emphasize the one proposed by Goldstein, Zebker, and Werner in 1988 [30], one of the earliest to be reported in the 2D phase unwrapping literature.

Choosing the placement for the branch cuts is a critical task, as illustrated in Fig. 3.3 taken from [31]. In Fig. 3.3(a) we show a set of opposite charges residues and a certain branch cuts configuration. Clearly, that is an ill choice, as there are large isolated regions which will always remain so<sup>5</sup>, and the lengthy branch cuts almost isolate other huge regions as well. The proposed configuration in Fig. 3.3(b) is clearly better, suggesting the minimization of the total branch cuts length as a criterion to the choice of the cuts configuration.

To minimize the total branch cuts length is, by itself, a very difficult problem. That is why Goldstein's algorithm only solves it approximately. Besides being seminal in the phase unwrapping literature, Goldstein's algorithm still is competitively fast and does not

<sup>4</sup>Also termed *residue cuts* by some authors.

<sup>5</sup>As integration paths cannot traverse branch cuts.

restrict itself to creating dipoles, but also residues clusters<sup>6</sup>. Other branch cuts algorithms include, e.g., [32], [33].

### 3.1.3 Quality Guided Algorithms

This class of algorithms employs quality maps to guide the integration paths. By noting that residues tend to be located in low quality regions of the image [31, Chap.4], they use the additional information, typically decorrelation maps, to avoid residues-originated path dependence without, however, explicitly identifying those residues. In fact, they constitute an attempt to overcome the possible misplacement of branch cuts which, as previously referred, is a difficult problem.

Many of these techniques basically adopt the criterion of letting the quality values to define the order by which phase is unwrapped, giving priority to high quality phase pixels [34], [35].

A further development is the conception of algorithms using quality maps to delineate the branch cuts [36], [37], [38]. In doing so, they attempt to employ the additional information contained in the quality maps, as well as retaining the branch cuts guarantee of path integration independence. When a good quality map is lacking, Goldstein's algorithm performance is found to be superior [31, Chap. 4].

Next we will briefly address the minimum norm methods.

## 3.2 Minimum Norm Methods

In the previous section, we introduced a key phase unwrapping class of methods which rely in path following concepts. Now, we will overview the other major approach to phase unwrapping: the minimum norm methods. As will become apparent in what follows, they rely on a completely different concept. While path following methods are local in nature, minimum norm methods adopt a global perspective, addressing the problem via optimization procedures that involve the image as a whole.

---

<sup>6</sup>More complex structures in which same charge residues are linked together forming charged clusters. The opposite charged clusters are then connected by a branch cut to balance charge.

### 3.2.1 The Minimum $L^p$ Norm

Minimum norm methods try to find an absolute phase image solution  $\Phi$  for which the  $L^p$  norm<sup>7</sup> of the difference (horizontal and vertical, respectively) between absolute phase derivatives and wrapped phase derivatives is minimized. We recall here that in digital image processing, the terms *derivative* and *linear difference* can be considered interchangeably<sup>8</sup>. This kind of methods, thus, look for unwrapped phase images whose local derivatives match the measured derivatives, in a certain sense that is given by the particular  $L^p$  norm chosen. So, in fact, they can be considered as surface fitting processes.

More formally, this minimization goal is to yield an unwrapped image solution  $\hat{\Phi}$ , and can be expressed by

$$\hat{\Phi} = \arg \min_{\Phi} E(\Phi), \quad (3.1)$$

with  $E(\Phi)$  being the above referred  $L^p$  norm which is given by

$$E(\Phi) = \sum_{m=1}^M \sum_{n=1}^{N-1} \left| \Delta^h \phi_{m,n} - \Delta^h \psi_{m,n} \right|^p + \sum_{m=1}^{M-1} \sum_{n=1}^N \left| \Delta^v \phi_{m,n} - \Delta^v \psi_{m,n} \right|^p, \quad p \geq 0 \quad (3.2)$$

and

$$\Delta^h \phi_{m,n} \equiv \phi_{m,n+1} - \phi_{m,n}, \quad \Delta^v \phi_{m,n} \equiv \phi_{m,n+1} - \phi_{m,n},$$

$$\Delta^h \psi_{m,n} \equiv \mathcal{W}(\psi_{m,n+1} - \psi_{m,n}), \quad \Delta^v \psi_{m,n} \equiv \mathcal{W}(\psi_{m,n+1} - \psi_{m,n}),$$

where,  $\Phi$  is a possible unwrapped image<sup>9</sup>,  $\Psi$  is the wrapped image,  $M$  and  $N$  denote, respectively, the images number of lines and columns,  $\Delta^h(\cdot)$  and  $\Delta^v(\cdot)$  denote the horizontal and vertical derivatives, respectively, and  $\mathcal{W}$  is the wrapper operator introduced in expression (2.15). Let us note here that the presence of the wrapper operator is, again, a way of applying the Itoh condition<sup>10</sup>. We emphatically stress that this is an optimization

<sup>7</sup>This is an analogy with norms defined in  $L^p$  spaces, which are measure theory concepts. For further reading see, e.g., [39].

<sup>8</sup>The term *linear difference* is employed here as the difference between neighbour pixels values.

<sup>9</sup>When referring to a whole image, instead of one of its pixels, we employ boldface types.

<sup>10</sup>To illustrate the importance of operator  $\mathcal{W}$  in this formula, let us consider two neighbour pixels with phase values  $\pi - 0.1$  and  $\pi + 0.1$ , respectively. Their correspondent derivative is  $\Delta = 0.2$ . On the other hand, their wrapped counterparts are  $\pi - 0.1$  and  $-\pi + 0.1$  respectively, and accordingly, their correspondent derivative is  $\Delta = -2\pi + 0.2$ . Obviously, it is desirable to fit the derivative of the unwrapped solution to the true  $\Delta = 0.2$  and not to  $\Delta = -2\pi + 0.2$ . It is, therefore, convenient to apply the wrapper operator to annihilate the erroneous introduced  $2\pi$  ambiguity in the latter derivative value.

problem constrained to integers, the constraints being given by  $\Phi = \Psi + 2\mathbf{k}\pi$ , where  $\mathbf{k}$  is an integer image, which is the difference between the unwrapped and the wrapped images,  $\Phi$  and  $\Psi$  respectively.

Furthermore, when a quality map (see Section 2.1.4)  $Q$  is available it is possible to derive horizontal and vertical quality measures [40]  $Q^h$  and  $Q^v$ , respectively<sup>11</sup>, and it can be defined a weighted  $L^p$  norm analogous to (3.2):

$$E(\Phi) = \sum_{m=1}^M \sum_{n=1}^{N-1} q_{m,n}^h \left| \Delta^h \phi_{m,n} - \Delta^h \psi_{m,n} \right|^p + \sum_{m=1}^{M-1} \sum_{n=1}^N q_{m,n}^v \left| \Delta^v \phi_{m,n} - \Delta^v \psi_{m,n} \right|^p, \quad p \geq 0. \quad (3.3)$$

In regions where it is known to exist absolute phase discontinuities, or noise corruption, we can set  $q_{m,n}$  to lower or zero values and, so, reduce the bad quality phase influence on the unwrapped solution [31, Chap. 4].

Expressions (3.1), (3.2), and (3.3) clearly highlight the global character of these techniques, in the sense that all the observed phases are used to compute a solution. Distinct exponent  $p$  values in  $L^p$  norms, yield distinct properties in the unwrapping performance; usually only  $p \leq 2$  values are employed and namely  $p = 0, 1, 2$  are the most representative. We will next quickly refer to some of the correspondent algorithms for these  $p$  values.

### 3.2.2 $L^2$ Norm Algorithms

With  $p = 2$ , we have a least squares problem. We remark here that the minimization of an  $L^p$  norm, as defined above, even just for  $p = 2$  is a discrete minimization problem which is very demanding from the computational point of view [31, Chap. 5]. As such, the great majority of the existing algorithms are approximate ones. In addition, a drawback of the  $L^2$  norm based criterion is that it tends to smooth discontinuities, unless they are provided as binary weights.

Fried and Hudgin were the first to propose least squares type phase unwrapping approximate algorithms [41], [42]. Since then, many algorithms have been published, from which we highlight (due to popularity) those approximating the least squares solution by relaxing the discrete domain  $\mathbb{Z}^{MN}$  to  $\mathbb{R}^{MN}$ <sup>12</sup>. In doing so, they intend to overcome the

<sup>11</sup>We can always define  $Q^h \equiv Q^v$ , in case we do not possess any further information.

<sup>12</sup>M and N denote the number of lines and columns, respectively.

complexity introduced by the discrete nature of the problem. It can be shown that in the continuous domain, the problem is equivalent to solving a Poisson partial differential equation [31, Chap. 5]. This has been solved by applying techniques using fast Fourier or cosine transforms, and then coming back to discrete domain [43]. An exact solution to least squares is developed as a step of the  $\mathbb{Z}\pi M$  algorithm in [6], using network programming techniques.

### 3.2.3 $L^1$ Norm Algorithms

$L^1$  norm performs better than  $L^2$  norm in what discontinuity preserving is concerned. Such a criterion has been solved exactly by Flynn [40] and Costantini [44], using network programming concepts. We here highlight with a little more detail Flynn's algorithm, as it is somehow closer to our own proposed algorithm.

#### Flynn's Minimum Discontinuity Algorithm

As introduced in Sections 2.2.1 and 2.2.2, phase unwrapping is an inverse problem with relation to the wrapping process, which in turn, by definition, creates discontinuities in the wrapped image. Given that the discontinuities in the unwrapped image should be limited to noisy areas and to the true absolute image discontinuities, which often can be identified in quality maps, Flynn's algorithm [40] fundamental idea consists in choosing between the possible unwrapped images (Section 2.2.1), the one which minimizes discontinuities. Basically, this algorithm operates by applying iteratively an elementary procedure of partitioning the image in two connected regions and, then, adding a  $2\pi$  phase to one of them, such that the weighted sum of discontinuities decreases.

Introducing, succinctly, the notation used by Flynn in [40], let us define, respectively, vertical and horizontal jump counts by:

$$v_{m,n} = \left\lfloor \frac{\phi_{m,n} - \phi_{m-1,n} + \pi}{2\pi} \right\rfloor, \quad (3.4)$$

$$z_{m,n} = \left\lfloor \frac{\phi_{m,n} - \phi_{m,n-1} + \pi}{2\pi} \right\rfloor, \quad (3.5)$$

where  $(m, n)$  represents the usual pixel indexing, and  $\lfloor x \rfloor$  is the largest integer less or

equal than  $x$ . A jump count is, then, the multiple of  $2\pi$  that is required to annihilate a discontinuity (we recall that a discontinuity exists when two neighbouring pixels phase difference is greater than  $\pi$ ). The goal of Flynn’s algorithm is, thus, to minimize

$$E = \sum w_{m,n}^v |v_{m,n}| + w_{m,n}^z |z_{m,n}|, \quad (3.6)$$

where  $w_{m,n}^v$  and  $w_{m,n}^z$  denote vertical and horizontal weights, respectively, which are derived from quality maps. It should be noted that the minimization procedure is guaranteed to reach the global minimum [40].

### 3.2.4 Low $p$ Valued $L^p$ Norm Algorithms

With  $0 \leq p < 1$  the discontinuity preserving ability of the minimum  $L^p$  norm algorithms is further increased at stake, however, of highly complex algorithms [45]. In particular,  $L^0$  norm is generally accepted as the most desirable in practice. The minimization of  $L^0$  norm is, however, an NP-hard problem<sup>13</sup> [46], [45], for which approximate algorithms have been proposed in [31, Chap. 5] and [47].

## 3.3 Bayesian and Parametric Methods

The Bayesian approach relies on a data-observation mechanism model, as well as a prior knowledge of the phase to be modelled. This is a probabilistic approach to phase unwrapping, where data-observation mechanism is modelled by a conditional probability density function  $P(\Psi|\Phi)$  and the *a priori* knowledge by the so-called prior probability density function  $P(\Phi)$ . Here  $\Phi$  is the unwrapped image and  $\Psi$  the wrapped image. Using the Bayes theorem

$$P(\Phi|\Psi) = \frac{P(\Psi|\Phi)P(\Phi)}{P(\Psi)}, \quad (3.7)$$

we can get the *a posteriori* probability density function and, from there, to infer the unwrapped image  $\Phi$ .

For instance in [48], a non-linear optimal filtering is applied, while in [49] an InSAR observation model is considered, taking into account not only the image phase, but also

---

<sup>13</sup>For algorithmic complexity theory issues see, e.g., [46].

the *backscattering coefficient* and *correlation factor* images, which are jointly recovered from InSAR image pairs. Work [50] proposes a fractal based prior.

Finally, parametric algorithms constrain the unwrapped phase to a parametric surface. Low order polynomial surfaces are used in [51]. Very often in real applications just one polynomial is not enough to describe accurately the complete surface. In such cases the image is partitioned and different parametric models are applied to each partition [51].

## Chapter 4

# The PUMF Approach

In this chapter we propose a new phase unwrapping method. Our approach is an energy minimization one that generalizes the classical minimum  $L^p$  norm formulation introduced in Section 3.2.

By changing into a more formal gear, we rigorously formulate the problem to be solved, develop the theoretical backgrounds of the proposed solution and, finally, present and discuss our phase unwrapping algorithm.

### 4.1 Problem Formulation

Figure 4.1 shows a site  $(i, j) \in \mathbb{Z}_0 \equiv \{(k, l) : k = 1, \dots, M, l = 1, \dots, N\}$  ( $\mathbb{Z}_0$  is the usual image pixel indexing 2D grid) and its first-order neighbours along with the variables  $h_{ij}$  and  $v_{ij}$  signalling horizontal and vertical discontinuities, respectively; i.e.  $h_{ij}, v_{ij} \in \{0, 1\}$  and  $h_{ij}, v_{ij} = 0$  signals a discontinuity.

Let us define the *energy*

$$E(\mathbf{k}|\boldsymbol{\psi}) \equiv \sum_{ij \in \mathbb{Z}_1} V(\Delta\phi_{ij}^h) v_{ij} + V(\Delta\phi_{ij}^v) h_{ij}, \quad (4.1)$$

where  $\mathbf{k} \equiv \{k_{ij} : (i, j) \in \mathbb{Z}_0\}$  is an integer image defined in  $\mathbb{Z}$ , of  $2\pi$  multiples, the so-called *wrap-count image*,  $\boldsymbol{\psi} \equiv \{\psi_{ij} : (i, j) \in \mathbb{Z}_0\}$  is the observed wrapped phase image,  $V(\cdot)$  is the *clique potential*, a real valued function, and  $(\cdot)^h$  and  $(\cdot)^v$  denote pixel horizontal and

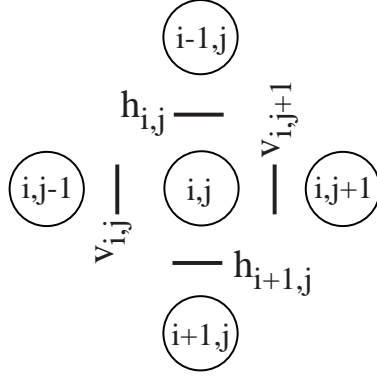


Figure 4.1: Representation of the site  $(i, j)$  and its first order neighbours along with the variables  $h_{ij}$  and  $v_{ij}$  signalling horizontal and vertical discontinuities respectively.

vertical differences given by

$$\Delta\phi_{ij}^h \equiv \left[ 2\pi(k_{ij} - k_{ij-1}) - \Delta\psi_{ij}^h \right], \quad k \in \mathbb{Z} \quad (4.2)$$

$$\Delta\phi_{ij}^v \equiv \left[ 2\pi(k_{ij} - k_{i-1j}) - \Delta\psi_{ij}^v \right], \quad k \in \mathbb{Z} \quad (4.3)$$

$$\Delta\psi_{ij}^h \equiv \psi_{ij-1} - \psi_{ij} \quad (4.4)$$

$$\Delta\psi_{ij}^v \equiv \psi_{i-1j} - \psi_{ij}, \quad (4.5)$$

and  $\mathbb{Z}_1 = \{(i, j) : i = 2, \dots, M, \quad j = 2, \dots, N\}$ .

Our goal is to find the integer image  $\mathbf{k}$  that minimizes energy (4.1),  $\mathbf{k}$  being such that  $\phi = 2\pi\mathbf{k} + \psi$ , where  $\phi$  is the estimated unwrapped phase image. As will be seen in the next section, this energy minimization approach yields the classical minimum  $L^p$  norm formulation or a more general one, depending on the clique potential  $V$ .

We should stress that the variables  $h_{ij}$  and  $v_{ij}$ , conveying discontinuity information, are introduced when available. In SAR jargon these images are the *quality maps*, briefly addressed in Section 2.1.4. These maps can also be used as continuous variables in  $[0, 1]$ , expressing prior knowledge on phase variability. Nevertheless, in practice, quality maps are often very noisy or unavailable, implying blind handling of discontinuities.

Although energy (4.1) was introduced deterministically in a natural way, it can also be derived under a Bayesian perspective, using a Markov random field as a prior; for more details see [6] and references therein.

## 4.2 Energy Minimization by a Sequence of Binary Optimizations

In this section, we present in detail the PUMF algorithm. We show that for convex potentials  $V$ , the minimization of  $E(\mathbf{k}|\boldsymbol{\psi})$  can be achieved through a sequence of binary optimizations; each binary problem is mapped onto a certain graph and a binary minimization obtained by computing a max-flow/min-cut on it. Finally, we address a set of potentials tailored to phase unwrapping.

### 4.2.1 An Existence Theorem for Energy Minimization

The following theorem is an extension of Lemma 1 taken from [6], which in turn is inspired by Lemma 1 of [40]. Assuming a convex clique potential  $V$ , it assures that if the minimum of  $E(\mathbf{k}|\boldsymbol{\psi})$  is not yet reached, then, there exists a binary image  $\delta\mathbf{k}$  (i.e., the elements of  $\delta\mathbf{k}$  are all 0 or 1) such that  $E(\mathbf{k} + \delta\mathbf{k}|\boldsymbol{\psi}) < E(\mathbf{k}|\boldsymbol{\psi})$ . The assumption of convexity is relaxed, in a certain sense, in Section 4.2.4.

**Theorem 1** *Let  $\mathbf{k}_1$  and  $\mathbf{k}_2$  be two wrap-count images such that*

$$E(\mathbf{k}_2|\boldsymbol{\psi}) < E(\mathbf{k}_1|\boldsymbol{\psi}). \quad (4.6)$$

*Then, if  $V$  is convex, there exists a binary image  $\delta\mathbf{k}$  such that*

$$E(\mathbf{k}_1 + \delta\mathbf{k}|\boldsymbol{\psi}) < E(\mathbf{k}_1|\boldsymbol{\psi}). \quad (4.7)$$

**Proof 1** *See the Appendix.*

According to Theorem 1, we can iteratively compute  $\mathbf{k}^{t+1} = \mathbf{k}^t + \delta\mathbf{k}$ , where  $\delta\mathbf{k} \in \{0, 1\}^{MN}$  minimizes<sup>1</sup>  $E(\mathbf{k}^t + \delta\mathbf{k}|\boldsymbol{\psi})$ , until the the minimum energy is reached.

---

<sup>1</sup>Or at least decreases.

## 4.2.2 Mapping Binary Optimizations onto Graph Max-Flows

Let  $k_{ij}^{t+1} = k_{ij}^t + \delta k_{ij}$  be the wrap-count at time  $t + 1$  and pixel  $(i, j)$ . Introducing  $k_{ij}^{t+1}$  into (4.2) and (4.3), we obtain, respectively,

$$\Delta\phi_{ij}^h = \left[ 2\pi(k_{ij}^{t+1} - k_{i-1j}^{t+1}) - \Delta\psi_{ij}^h \right] \quad (4.8)$$

$$\Delta\phi_{ij}^v = \left[ 2\pi(k_{ij}^{t+1} - k_{i-1j}^{t+1}) - \Delta\psi_{ij}^v \right]. \quad (4.9)$$

After some simple manipulation, we get

$$\Delta\phi_{ij}^h = \left[ 2\pi(\delta k_{ij} - \delta k_{i-1j}) + a^h \right] \quad (4.10)$$

$$\Delta\phi_{ij}^v = \left[ 2\pi(\delta k_{ij} - \delta k_{i-1j}) + a^v \right], \quad (4.11)$$

where

$$a^h \equiv 2\pi(k_{ij}^t - k_{i-1j}^t) - \Delta\psi_{ij}^h \quad (4.12)$$

$$a^v \equiv 2\pi(k_{ij}^t - k_{i-1j}^t) - \Delta\psi_{ij}^v. \quad (4.13)$$

Now, introducing (4.10) and (4.11) into (4.1), we can rewrite energy  $E(\mathbf{k}^t + \delta\mathbf{k}|\boldsymbol{\psi})$  as a function of the binary variables  $\delta k_{ij} \in \{0, 1\}$ , i.e.,

$$E(\mathbf{k}^t + \delta\mathbf{k}|\boldsymbol{\psi}) = \sum_{ij \in \mathbb{Z}_1} V \underbrace{\left[ 2\pi(\delta k_{ij} - \delta k_{i-1j}) + a^h \right]}_{E_h^{ij}(x_{i-1j}, x_{ij})} v_{ij} + \underbrace{V \left[ 2\pi(\delta k_{ij} - \delta k_{i-1j}) + a^v \right]}_{E_v^{ij}(x_{i-1j}, x_{ij})} h_{ij}, \quad (4.14)$$

where  $x_{ij} \equiv \delta k_{ij}$ . Occasionally, and for the sake of notational simplicity, we use the representation,

$$E(\mathbf{k}^t + \mathbf{x}|\boldsymbol{\psi}) = \sum_{ij \in \mathbb{Z}_1} E^{ij}(x_i, x_j), \quad (4.15)$$

where indices  $i, j$  correspond now to the lexicographic column ordering<sup>2</sup> of  $\mathbb{Z}_0$ ,  $x_i \in \{0, 1\}$ , and  $\mathbf{x} = \{x_i\} \in \{0, 1\}^{MN}$ . Notice that with this representation some terms  $E^{ij}$  stand for

---

<sup>2</sup>Lexicographic ordering corresponds to the dictionary ordering. More formally: Given  $A$  and  $B$ , two ordered sets, the lexicographical order in the cartesian product  $A \times B$  is defined as  $(a, b) \leq (a', b')$  iff  $a' < a$ , or  $a = a'$  and  $b' \leq b$ .

horizontal clicks whereas others stand for vertical ones (e.g.,  $E^{12}$  and  $E^{1(M+1)}$  represent vertical and horizontal clicks, respectively).

The minimization of (4.14) with respect to  $\delta \mathbf{k}$  is now mapped onto a max-flow problem. Since the seminal work of Greig et al. [52], a considerable amount of research effort has been devoted to energy minimization via graph methods (see, e.g., [7], [53], [54], [55], [56], [57]). Namely, the mapping of a minimization problem into a sequence of binary minimizations, computed by graph cut techniques, has been addressed in works [53] and [54]. Nevertheless, these two works assume the potentials to be either a metric or a semi-metric, which is not the case for the clique potentials that we are considering: from (4.14), it can be seen that  $E^{ij} \neq E^{ji}$  as a consequence of the presence of  $a^h$  and  $a^v$  terms<sup>3</sup>. For this reason, we adopt the method proposed in [7], which generalizes the class of binary minimizations that can be solved by graph cuts. Furthermore, the graph structures therein proposed are simpler.

At this point a reference to work [57] should be made: it introduces an energy minimization for convex potentials also by computing a max-flow/min-cut on a certain graph. However, for a general convex potential that graph can be huge, imposing in practice, heavy computational and storage demands.

Following, then, [7], we now exploit a one-to-one map existing between the energy function (4.14) and cuts on a directed graph  $\mathcal{G} = (\mathcal{V}, \mathcal{E})$  ( $\mathcal{V}$  and  $\mathcal{E}$  denote the set of vertices and edges, respectively) with non-negative weights. The graph has two special vertices, namely the source  $s$  and the sink  $t$ . An  $s - t$  cut  $C = S, T$  is a partition of vertices  $\mathcal{V}$  into two disjoint sets  $S$  and  $T$ , such that  $s \in S$  and  $t \in T$ . The number of vertices is  $2 + M \times N$  (two terminals, the source and the sink, plus the number of pixels). The cost of the cut is the sum of costs of all edges between  $S$  and  $T$ .

Using the notation introduced in (4.15), we have

$$\begin{aligned}
 E^{ij}(0, 0) &= V(a) d_{ij}, \\
 E^{ij}(1, 1) &= V(a) d_{ij}, \\
 E^{ij}(0, 1) &= V(-2\pi + a) d_{ij}, \\
 E^{ij}(1, 0) &= V(2\pi + a) d_{ij},
 \end{aligned}
 \tag{4.16}$$

---

<sup>3</sup>By definition both a metric and a semi-metric satisfy the symmetry property.

where  $a$  represents  $a_h$  or  $a_v$  and  $d_{ij}$  represents  $h_{ij}$  or  $v_{ij}$ . Energy  $E(\mathbf{k}^t + \mathbf{x}|\boldsymbol{\psi})$  is a particular case of the  $\mathcal{F}^2$  class of functions addressed in [7], with zero unary terms. A function of  $\mathcal{F}^2$  is *graph representable*, i.e., roughly speaking<sup>4</sup>, there exists a one-to-one relation between configurations  $\mathbf{x} \in \{0, 1\}^{MN}$  [i.e., points in the domain of  $E(\mathbf{k}^t + \mathbf{x}|\boldsymbol{\psi})$ ] and  $s - t$  cuts on that graph, if and only if  $E^{ij}(0, 0) + E^{ij}(1, 1) \leq E^{ij}(0, 1) + E^{ij}(1, 0)$ .

In the proof of Theorem 1 (see the Appendix), we derived the inequality

$$V(a) + V(c) - V(b) \geq V(a + c - b), \quad (4.17)$$

for any real triplet  $a, b, c$  such that  $\min(a, c) \leq b \leq \max(a, c)$ . So, in particular,

$$V(-2\pi + a) + V(2\pi + a) - V(a) \geq V[2\pi + a + (-2\pi + a) - a] \quad (4.18)$$

$$V(-2\pi + a) + V(2\pi + a) \geq 2V(a) \quad (4.19)$$

$$[V(-2\pi + a) + V(2\pi + a)] d_{ij} \geq 2V(a)d_{ij}, \quad (4.20)$$

which, in terms of  $E^{ij}$  [see expression (4.16)], can be stated as

$$E^{ij}(0, 0) + E^{ij}(1, 1) \leq E^{ij}(0, 1) + E^{ij}(1, 0). \quad (4.21)$$

So, our binary function is graph-representable.

The structure of the graph is as follows: first build vertices and edges corresponding to each pair of neighbouring pixels, and then join these graphs together based on the additivity theorem also given in [7].

So, for each energy term  $E_h^{ij}$  and  $E_v^{ij}$  [see expression (4.14)], we construct an “elementary” graph with four vertices  $\{s, t, v, v'\}$ , where  $\{s, t\}$  represents source and the sink, common to all terms, and  $\{v, v'\}$  represents the two pixels involved [ $v$  being the left (up) pixel and  $v'$  the right (down) pixel]. Following very closely [7], we define a directed edge  $(v, v')$  with the weight  $E(0, 1) + E(1, 0) - E(0, 0) - E(1, 1)$ . Moreover, if

---

<sup>4</sup>As defined in [7], a function  $E$  of  $n$  binary variables is called *graph-representable* if there exists a graph  $\mathcal{G} = (\mathcal{V}, \mathcal{E})$  with terminals  $s$  and  $t$  and a subset of vertices  $\mathcal{V}_0 = \{v_1, \dots, v_n\} \subset \mathcal{V} - \{s, t\}$  such that, for any configuration  $x_1, \dots, x_n$ , the value of the energy  $E(x_1, \dots, x_n)$  is equal to a constant plus the cost of the minimum  $s$ - $t$ -cut among all cuts  $C = S, T$  in which  $v_i \in S$ , if  $x_i = 0$ , and  $v_i \in T$ , if  $x_i = 1$  ( $1 \leq i \leq n$ ).

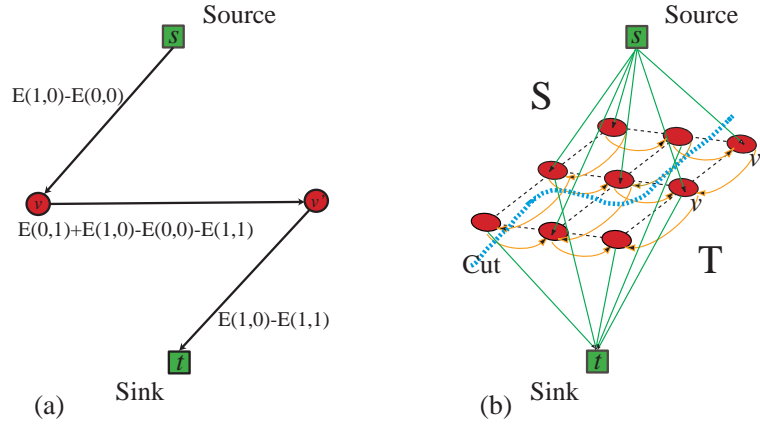


Figure 4.2: (a) Elementary graph for a single energy term, where  $s$  and  $t$  represent source and sink, respectively, and  $v$  and  $v'$  represent the two pixels involved in the energy term. In this case  $E(1,0) - E(0,0) > 0$  and  $E(1,0) - E(1,1) > 0$ . (b) The graph obtained at the end results from adding elementary graphs.

$E(1,0) - E(0,0) > 0$ , we define an edge  $(s, v)$  with the weight  $E(1,0) - E(0,0)$  or, otherwise, we define an edge  $(v, t)$  with the weight  $E(0,0) - E(1,0)$ . In a similar way for vertex  $v'$ , if  $E(1,1) - E(1,0) > 0$ , we define an edge  $(s, v')$  with weight  $E(1,1) - E(1,0) > 0$  or, otherwise, we define an edge  $(v', t)$  with the weight  $E(1,0) - E(1,1)$ . Figure 4.2(a) shows an example where  $E(1,0) - E(0,0) > 0$  and  $E(1,0) - E(1,1) > 0$ . Figure 4.2(b) illustrates the complete graph obtained at the end.

### 4.2.3 Energy Minimization Algorithm

In this section we propose an algorithm that implements the PUMF approach.

---

**Algorithm 1** PUMF: Graph cuts based phase unwrapping algorithm.

---

**Initialization:**  $\mathbf{k} \equiv \mathbf{k}' \equiv \mathbf{0}$ , possible\_improvement  $\equiv 1$

```

1: while possible_improvement do
2:   Compute  $E(0, 0)$ ,  $E(1, 1)$ ,  $E(0, 1)$ , and  $E(1, 0)$  {for every horizontal and vertical pixel pair}.
3:   Construct elementary graphs and merge them to obtain the main graph.
4:   Compute the max-flow/min-cut  $(S, T)$  { $S$ - source set;  $T$ -sink set}.
5:   for all pixel  $(i, j)$  do
6:     if pixel  $(i, j) \in S$  then
7:        $\mathbf{k}'_{i,j} = \mathbf{k}_{i,j} + 1$ 
8:     else
9:        $\mathbf{k}'_{i,j} = \mathbf{k}_{i,j}$  {remains unchanged}
10:    end if
11:  end for
12:  if  $E(\mathbf{k}'|\psi) < E(\mathbf{k}|\psi)$  then
13:     $\mathbf{k} = \mathbf{k}'$ 
14:  else
15:    possible_improvement = 0
16:  end if
17: end while

```

---

Algorithm 1 shows the pseudo-code for the Phase Unwrapping Max-Flow (PUMF) algorithm. It solves a sequence of binary optimizations until no energy decreasing is possible. An essential question is whether the number of binary optimizations is finite, and so the algorithm terminates. Consider that the sequence  $\mathbf{k}^t$  takes values in  $\mathcal{C} = \{0, \dots, k_{max}\}^{MN}$ , where  $k_{max}$  is the maximum admitted wrap-count. Since the set  $\{\mathbf{k} : \mathbf{k} \in \mathcal{C}\}$  is finite, then, necessarily any strictly energy decreasing path on  $\mathcal{C}$  does have a finite length, and PUMF does have a finite number of steps, i.e., it terminates.

Concerning computational complexity, PUMF takes  $N_{bopt} \times N_{mf}$  flops (measured in number of floating point operations), where  $N_{bopt}$  and  $N_{mf}$  stand for number of binary optimizations and number of flops per max-flow computation, respectively.

Although the number of binary optimizations depends on the specific problem at hand, we have found out empirically that  $N_{bopt} \simeq \lceil (\max_{ij}(\phi_{ij}) - \min_{ij}(\phi_{ij})) / (2\pi) \rceil^5$ . Assuming that the initial phase is zero everywhere, a crude explanation for this number is that after

---

<sup>5</sup>Where  $\phi_{ij}$  stands for the unwrapped image.

$k$  binary optimization steps, the algorithm correctly finds any wrap-count less or equal than  $k$ .

In the results presented in section 5, we have used the augmenting path type max-flow/min-cut algorithm proposed in [58]. The worst case complexity for augmenting path algorithms is  $O(n^2m)$  [59], where  $n$  and  $m$  are the number of vertices and edges, respectively. However, in a huge array of experiments conducted in [58], authors systematically found out a complexity that is inferior to that of the push-relabel algorithm [60], with the queue based selection rule, which is  $O(n^2\sqrt{m})$ . Thus, we herein take this bound.

Given that in our graphs  $m \simeq 3n$  and  $N_{\text{bopt}}$  does not depend on  $n$ , the worst case complexity of the PUMF algorithm is bounded above by  $O(n^{2.5})$ . In section 5, we run a set of experiments where the worst case complexity is roughly  $O(n)$ . This scenario has systematically been observed.

#### 4.2.4 Clique Potentials

So far, we have assumed the clique potentials to be convex. This is central in the two main results in the thesis: the Theorem 1 and the regularity of energy (4.1). Both are implied by the inequality (A.11)

$$V(a) + V(c) - V(b) \geq V(a + c - b), \quad (4.22)$$

shown in Appendix, where  $\min(a, c) \leq b \leq \max(a, c)$ .

What if we apply a function  $\theta$  to the arguments of  $V$ ? Using the notation  $\theta(x) = x'$ , we get the proposition:

$$V(a') + V(c') - V(b') \geq V[(a + c - b)']. \quad (4.23)$$

Now, noting that, by construction<sup>6</sup>,  $a, b$  and  $c$  differ from each other by multiples of  $2\pi$ , if we choose  $\theta(x) = \mathcal{P}(x) + \alpha x$ , where  $\mathcal{P}$  is any  $2\pi$ -periodic real valued function and  $\alpha \in \mathbb{R}$ ,

---

<sup>6</sup>Stated in the proof of Theorem 1.

proposition (4.23) becomes,

$$V(a') + V(c') - V(b') \geq V[\mathcal{P}(a + c - b) + \alpha(a + c - b)] \quad (4.24)$$

$$= V[\mathcal{P}(a) + \alpha(a + c - b)] \quad (4.25)$$

$$= V[(\mathcal{P}(a) + \alpha a) + (\mathcal{P}(a) + \alpha c) - (\mathcal{P}(a) + \alpha b)] \quad (4.26)$$

$$= V(a' + c' - b'). \quad (4.27)$$

Since any  $2\pi$ -sampling of  $\theta$  is a monotone sequence, it is guaranteed that  $\min(a', c') \leq b' \leq \max(a', c')$ ; so, proposition (4.27) follows from expression (4.22). Therefore we have the following result:

**Proposition 1** *The set of clique potentials considered in Theorem 1 can be enlarged by admitting functions of the form  $V \equiv C \circ (P + L)$ , where  $C$  is a convex function,  $P$  is a  $2\pi$ -periodic function, and  $L$  is a linear function.*

It should be stressed that for such a potential, the regularity condition (4.21) is also satisfied; it follows directly from (4.27). We can thus conclude that the PUMF algorithm is valid for this broader class of clique potential functions. We next give two examples of possible clique potentials.

### The classical $L^p$ norm

This norm, corresponds, by far, to the most widely used phase unwrapping methods; recalling section 3.2, we can see that it is given by  $V(\Delta\phi) = |\Delta\phi - \mathcal{W}(\Delta\psi)|^p$ , where  $\mathcal{W}(x)$  is the wrapper operator defined by (2.15) and, thus,  $\mathcal{W}(x) \in ]-\pi \pi]$ . Since  $\Delta\phi$  and  $\Delta\psi$  differ by a multiple of  $2\pi$ , then  $|\Delta\phi - \mathcal{W}(\Delta\psi)|^p = |\Delta\phi - \mathcal{W}(\Delta\phi)|^p$ . Therefore, in our setting, we identify immediately  $C(x) = |x|^p$ ,  $\mathcal{P}(x) = -\mathcal{W}(x)$ , and  $A(x) = x$ .

Again recalling section 3.2, methods using this clique potential find a phase solution  $\phi$  for which  $L^p$  norm of the difference between absolute phase differences and wrapped phase differences (so a second order difference) is minimized.

From above, we see that  $C(x)$  is convex given that  $p \geq 1$ . Therefore, we conclude that, for this range of  $p$  values, PUMF exactly solves the classical minimum  $L^p$  norm phase unwrapping problem.

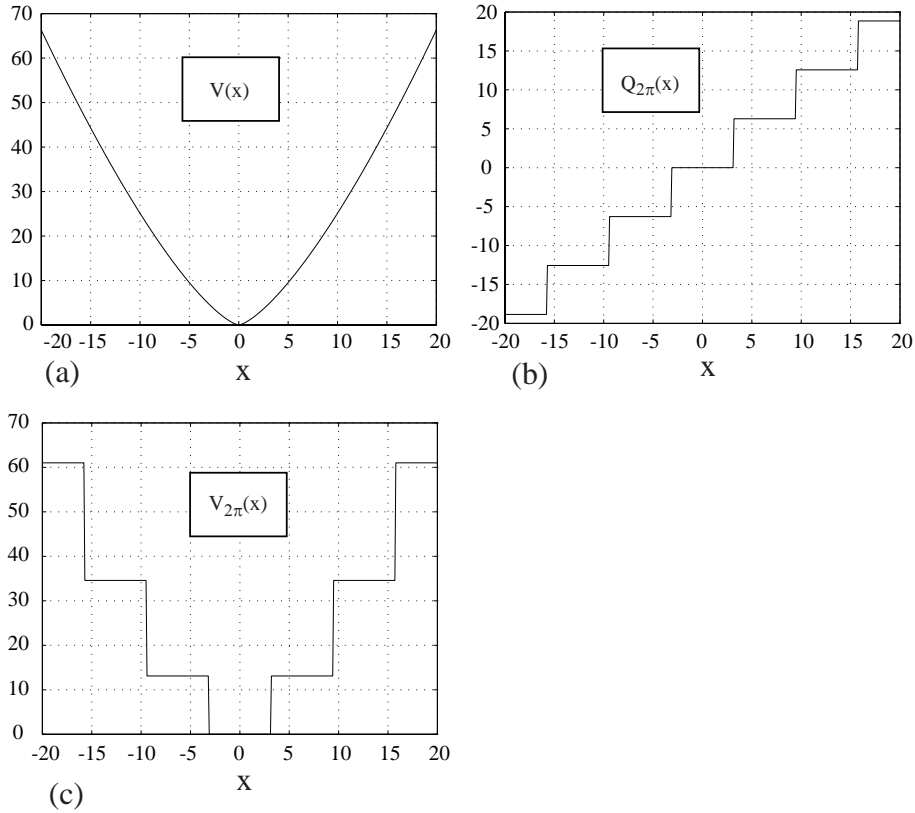


Figure 4.3: (a) The convex function  $C(x) = |x|^{1.4}$ ; (b)  $Q_{2\pi}(x) = x - \mathcal{W}(x)$ ; (c) The classical  $L^{1.4}$  norm potential given by  $V_{2\pi}(x) = C[Q_{2\pi}(x)]$ .

We refer to  $Q_{2\pi}(x) \equiv -\mathcal{W}(x) + x$  as the  $2\pi$ -quantization function and denote  $V_{2\pi}(x) \equiv V[Q_{2\pi}(x)]$ .

Figure 4.3 plots the potential  $C(x) = |x|^{1.4}$ , the quantization function  $Q_{2\pi}(x)$ , and the classical  $L^{1.4}$  norm given by  $V_{2\pi}(x) = |Q_{2\pi}(x)|^{1.4}$ .

### Convex potential

Choosing any convex  $C(x)$ ,  $P(x) = 0$  and  $L(x) = x$ , we obviously get back to the convex potential case. For example, the quadratic clique potential  $V(x) = x^2$  was used in work [6], under a Bayesian approach and a Markovian prior for the absolute phase. As already said, this potential tends to wash out phase discontinuities.

## Chapter 5

# PUMF Performance

In this chapter we illustrate the PUMF performance on a set of representative phase unwrapping problems. The data employed is distributed with book [31] and is widely adopted as a testbed for PU algorithms performance evaluation. In addition, we also benchmark PUMF against the main state-of-the-art algorithms.

The results presented for PUMF were obtained with MATLAB coding (max-flow algorithm is implemented in C++<sup>1</sup>), and using a PC workstation equipped with a 1.7 Ghz Pentium-IV CPU. The benchmark algorithms are coded in C and also distributed with [31].

### 5.1 Gaussian Hills

Figures 5.1 (a) and 5.1 (b) display two phase images ( $100 \times 100$  pixels) to be unwrapped; they are synthesized from an original absolute phase surface formed by a Gaussian elevation with a height of  $14\pi$  rad, and standard deviations  $\sigma_i = 10$  and  $\sigma_j = 15$  pixels, in the horizontal and vertical dimensions, respectively. The wrapped images are generated according to an InSAR observation statistics (see, e.g., [6]), producing an interferometric pair, with correlation coefficient 1.0 and 0.95, respectively. This corresponds to an interferometric noise standard deviation of  $0^\circ$  and  $50.5^\circ$ , respectively. The wrapped phase images are obtained (for each pair), by computing the product of one image by the com-

---

<sup>1</sup>Code made available at <http://www.cs.cornell.edu/People/vnk/software.html> by V. Kolmogorov. See [58] for more details.

plex conjugate of the other, and finally taking the argument. The noise standard deviation of  $50.5^\circ$  is large enough to induce a huge number of residues, making the unwrapping a hard task. Figures 5.1 (c) and 5.1 (d) show the corresponding unwrapped surfaces by PUMF using a non-quantized (see section 4.2.4)  $L^2$  norm potential. We can see that, even with low-correlation induced discontinuities, PUMF successfully accomplishes a meaningful unwrapping. Figures 5.1 (e) and 5.1 (f) show the energy evolution along the nine iterations taken by the algorithm to perform the unwrapping. It is noticeable a major energy decreasing in the first few iterations. We point out that it was not supplied any discontinuity information to the algorithm.

As referred in Section 4.2.3, we have observed approximately an  $O(n)$  complexity (where  $n$  is the size of the input image) in the experiences we have run with PUMF. Figure 5.2 illustrates this for the unwrapping of the Gaussian surface with and without noise, and employing two kinds of clique potentials.

Figure 5.3 (a) is analogous to 5.1 (a), but now the original absolute phase surface Gaussian elevation has a quarter set to zero. This introduces additional discontinuities in the wrapped values, therefore rendering a quite difficult unwrapping problem. We remark here that, again, no discontinuities are explicitly supplied in this application example, i.e., no quality maps are supplied to the algorithm. In Fig. 5.3 (b) we show the unwrapped solution with a classical  $L^2$  potential, which clearly is useless<sup>2</sup>. A successful unwrapping was obtained with a quantized potential, the classical  $L^1$ , and the result is shown in Fig. 5.3 (c); this result illustrates the ability of PUMF to cope with absolute phase discontinuities, when low  $p$  values are used. In Figs. 5.3 (d) and 5.3 (e) we display, respectively, a 3-D representation of the unwrapped solution and the energy evolution along the nine iterations taken by the algorithm to achieve the correct solution.

## 5.2 Shear Ramps

Figures 5.4 (a) and 5.4 (b) display two phase images to be unwrapped; they are synthesized from an original absolute phase surface formed by two equal size planes with slopes 0 and 1 rad/pixel (maximum height is 99 rad). The wrapped images are generated using the same

---

<sup>2</sup>The non-quantized version (section 4.2.4) yields a similarly useless solution.

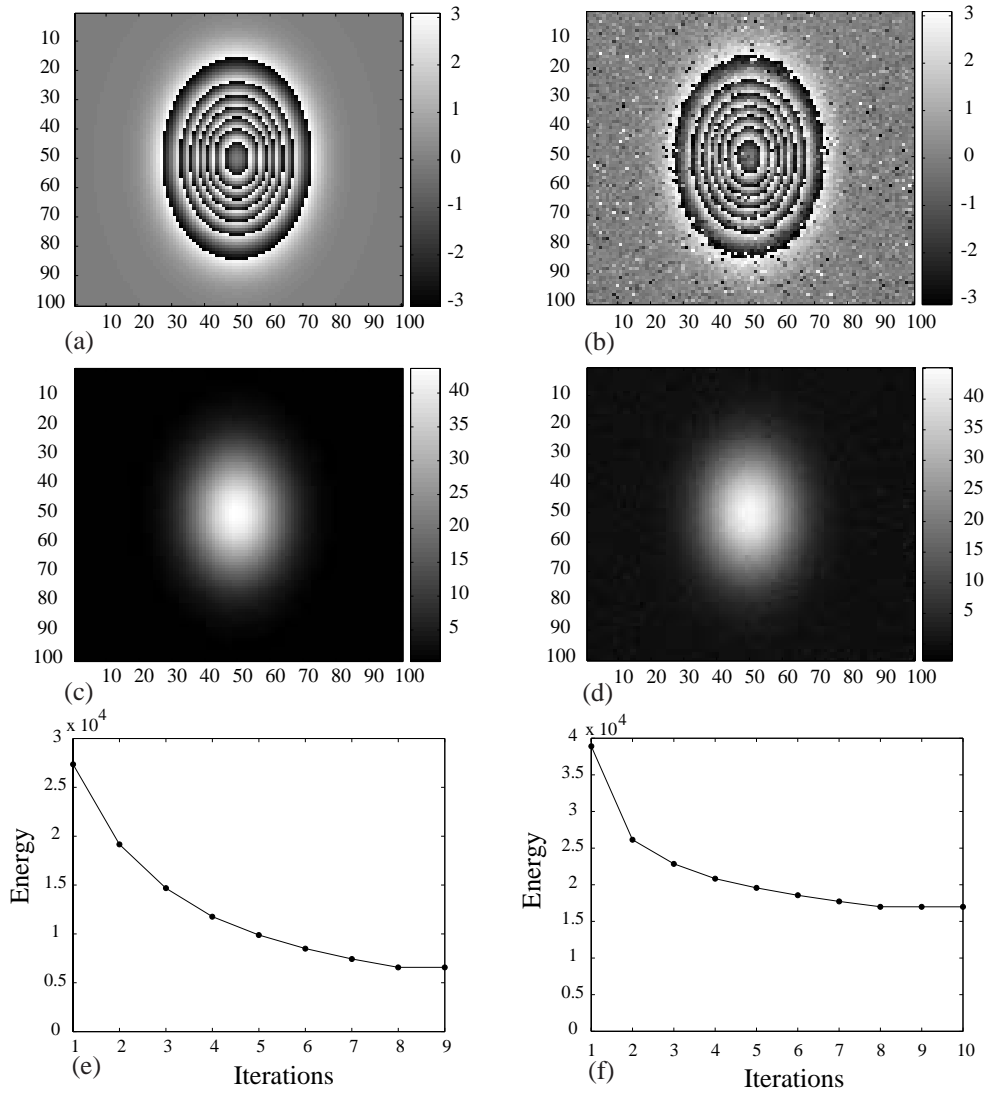


Figure 5.1: (a) Wrapped Gaussian elevation with  $14\pi$  height; correspondent colorbar on the right. The associated noise standard deviation is  $0^\circ$ . (b) Wrapped Gaussian elevation with  $14\pi$  height; correspondent colorbar on the right. The associated noise standard deviation is  $50.5^\circ$ . (c) Image in (a) unwrapped by PUMF; correspondent colorbar on the right. (d) Image in (b) unwrapped by PUMF; correspondent colorbar on the right. (e) Energy decreasing for the unwrapping of image in (a). (f) Energy decreasing for the unwrapping of image in (b).

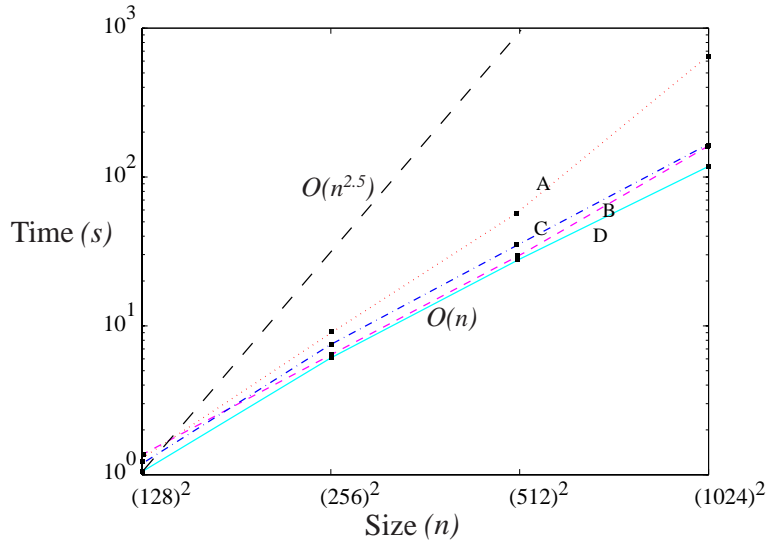


Figure 5.2: Unwrapping times of a  $14\pi$  height Gaussian surface with PUMF, using a PC workstation equipped with a 1.7 Ghz Pentium-IV CPU: time ( $s$ ) vs image size ( $n$ ). Time grows roughly as  $O(n)$  in all the four shown experiments. An  $O(n^{2.5})$  line is shown for reference. (A) Gaussian surface with  $50.5^\circ$  interferometric noise unwrapped with a non-quantized  $L^2$  norm. (B) Gaussian surface without interferometric noise unwrapped with a non-quantized  $L^2$  norm. (C) Gaussian surface with  $50.5^\circ$  interferometric noise unwrapped with a classical (quantized)  $L^2$  norm. (D) Gaussian surface without interferometric noise unwrapped with a classical (quantized)  $L^2$  norm.

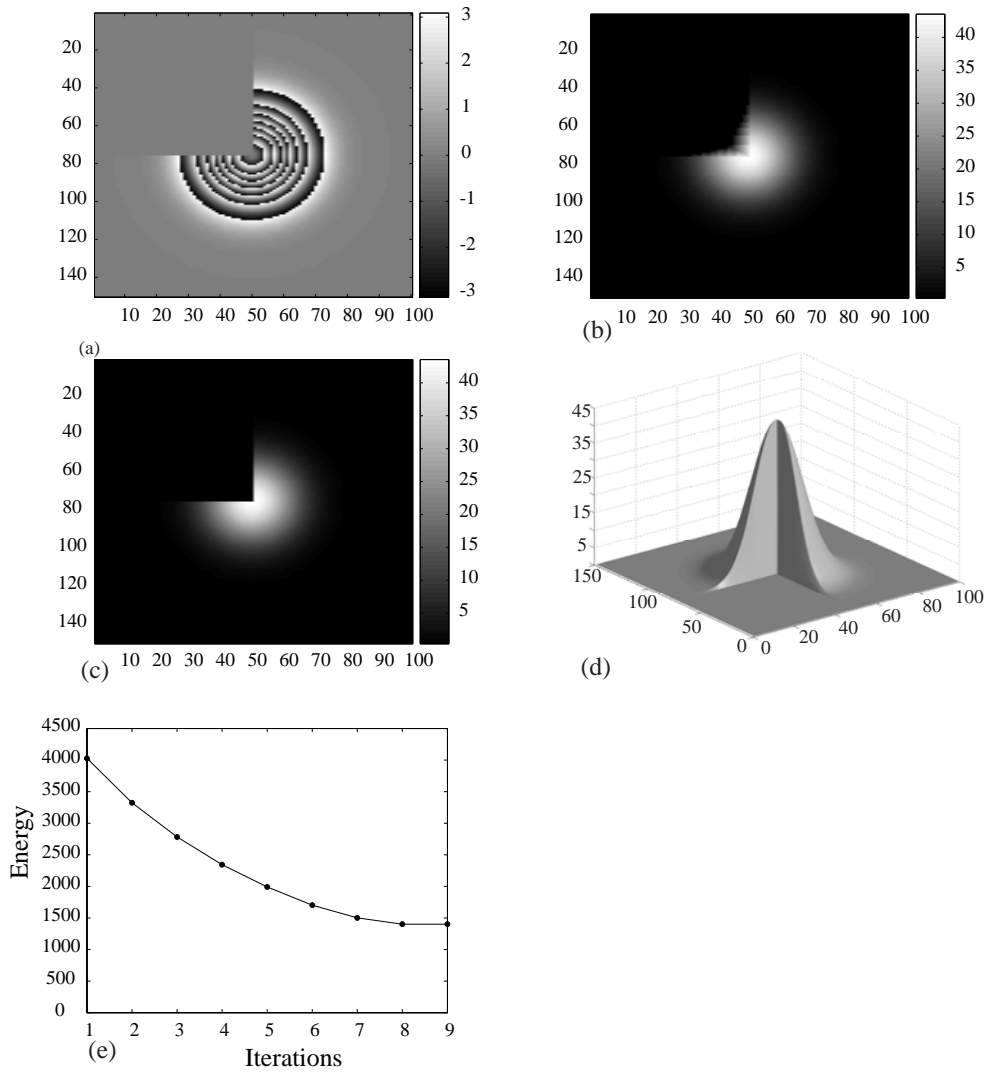


Figure 5.3: (a) Wrapped Gaussian elevation with  $14\pi$  height and a quarter set to zero; correspondent colorbar on the right. The associated noise standard deviation is  $0^\circ$ . (b) Failed unwrapping of the image in (a); correspondent colorbar on the right. It was employed a (quantized)  $L^2$  norm. (c) Image in (a) successfully unwrapped by PUMF; correspondent colorbar on the right. It was employed a (quantized)  $L^1$  norm. (d) 3-D representation of the unwrapped image. (e) Energy decreasing along the unwrapping process.

procedure described for images in 5.1 (a) and (b), again with interferometric noise standard deviation of  $0^\circ$  and  $50.5^\circ$ , respectively. The main unwrapping difficulty with these images, lies in the shear line that separates the two equal size planes, which is an obvious source of discontinuities; once more no quality maps are used to supply explicit discontinuities information. We note, again, that the  $50.5^\circ$  noise standard deviation is high enough to also induce a large number of phase residues, making the unwrapping even harder. Figures 5.4(c) and 5.4(d) show the corresponding unwrapped surfaces by PUMF using a classical  $L^1$  norm, both taking 18 iterations. We can see that, even with low-correlation induced discontinuities, PUMF successfully accomplishes a meaningful unwrapping. Figures 5.4 (e) and (f) display, respectively, the corresponding energy evolutions. Figure 5.4 (g) displays a 3-D representation of the unwrapped image in (c). Finally, Fig. 5.4 (h) shows the failed unwrapping of the image in 5.4 (b) with a classical  $L^{1.5}$  potential. As expected, the failure is mainly along the shear line where the major discontinuities lie. This, over again, highlights the PUMF ability to preserve discontinuities and the importance of a low  $p$  value to do it.

### 5.3 Long’s Peak

In this section we apply PUMF to InSAR data. The interferogram phase image is distributed with [31], and was obtained from a USGS<sup>3</sup> digital elevation model, by using a high-fidelity InSAR simulator [31, Chap. 3] (for more information see the references therein). Geographically, the data corresponds to Long’s Peak, in Colorado (USA), which is a steep-relief terrain thus inducing phase discontinuities and posing a challenging phase unwrapping problem. Moreover, the simulator introduces shadowing, layover, and speckle noise, which constitute well known characteristic SAR imaging phenomena [4]: shadowing results from the absence of radar echoes of terrain areas that are occluded by other terrain areas; layover is quite the opposite, as it corresponds to coincident echoes from different terrain areas; speckle noise is characteristic of coherent imaging systems, and is due to interference of the echoes returned from the scatterers, that are within the same resolution cell.

---

<sup>3</sup>United States Geological Survey.

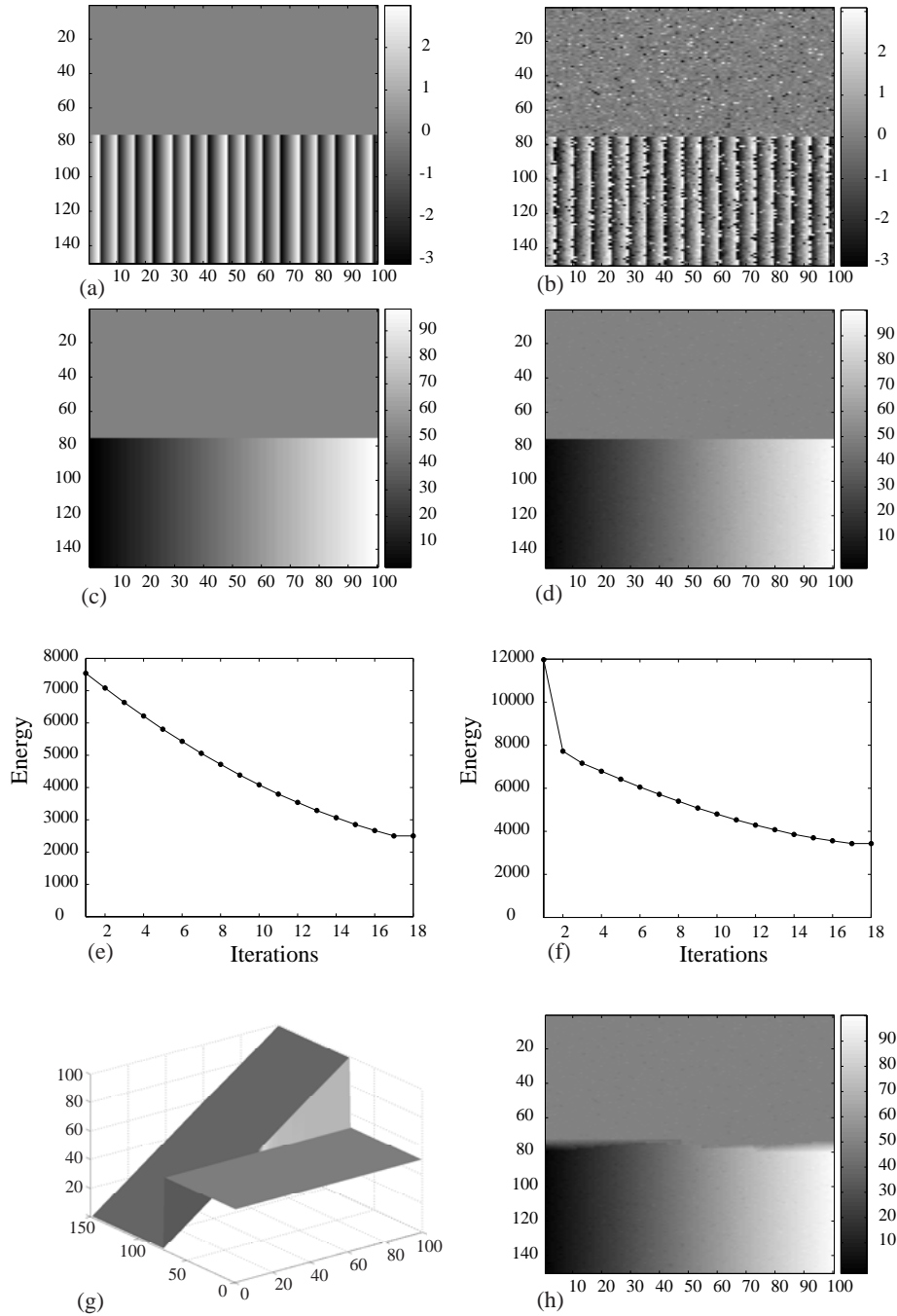


Figure 5.4: (a) Wrapped shear planes without noise; correspondent colorbar on the right. The associated noise standard deviation is  $0^\circ$ . (b) Wrapped shear planes with noise ( $50.5^\circ$  standard deviation); colorbar on the right. (c) Image in (a) successfully unwrapped by PUMF using a classical  $L^1$  norm; colorbar on the right. (d) Image in (b) successfully unwrapped by PUMF using a classical  $L^1$  norm; colorbar on the right. (e) Energy decreasing for the unwrapping of image in (a). (f) Energy decreasing for the unwrapping of image in (b). (g) 3-D representation of the unwrapped image in (c). (h) Failed unwrapping of the image in (b); colorbar on the right. It was employed a classical  $L^{1.5}$  norm.

In Fig. 5.5 (a) we depict a contour map (values in radians) corresponding to the Long’s Peak DEM and in Fig. 5.5 (b) we show the corresponding interferogram phase image. In this wrapped image, the regions where the fringes come very close each other, correspond to layover [31, Chap.3]. The black areas at top and bottom correspond to artifacts. Figure 5.5 (c) displays a quality map computed from the InSAR coherence estimate [31, Chap.4], while Fig. 5.5 (d) presents a subset of that quality map; this subset was supplied as a discontinuity information to PUMF; this reduced quality map usage, aims at somehow suggesting the PUMF ability to preserve discontinuities. Finally, Fig. 5.5 (e) displays a 3-D rendering of the resulting phase unwrapping, showing the Long’s Peak; a non-quantized  $L^1$  potential was used. Figure 5.5 (f) depicts the energy decreasing for the unwrapping along the 23 iterations employed to accomplish phase unwrapping.

## 5.4 Benchmarking

In this section we benchmark PUMF against main state-of-the-art algorithms, using the above presented PUMF phase unwrapping examples. The algorithms performances are measured by the standard deviation of the absolute error between original and unwrapped phase images<sup>4</sup>. The results are summarized in tables 5.1, 5.2, and 5.3 corresponding, respectively, to the examples shown in sections 5.1, 5.2, and 5.3. It should be noted that only in the latter we provide discontinuity information, by supplying the binary quality map, displayed in Fig. 5.5 (d), to all competing algorithms. In this case, we do not include the areas masked out by this quality map, as well as the above referred top and bottom artifact areas, in the computation of the error measure.

The comparing algorithms are:

- **Path following type:** Goldstein’s branch cut (GBC) [30]; quality guided (QG) [61]; and mask cut (MC) [38].
- **Minimum norm type:** Flynn’s minimum discontinuity (FMD) [40]; weighted least-squares (WLS) [43]; and  $L^0$  norm (L0N) (see [31, Chap. 5.5]).

---

<sup>4</sup>The absolute error is the difference between the images. The difference is defined pixel-to-pixel, and so the absolute error is itself an image.

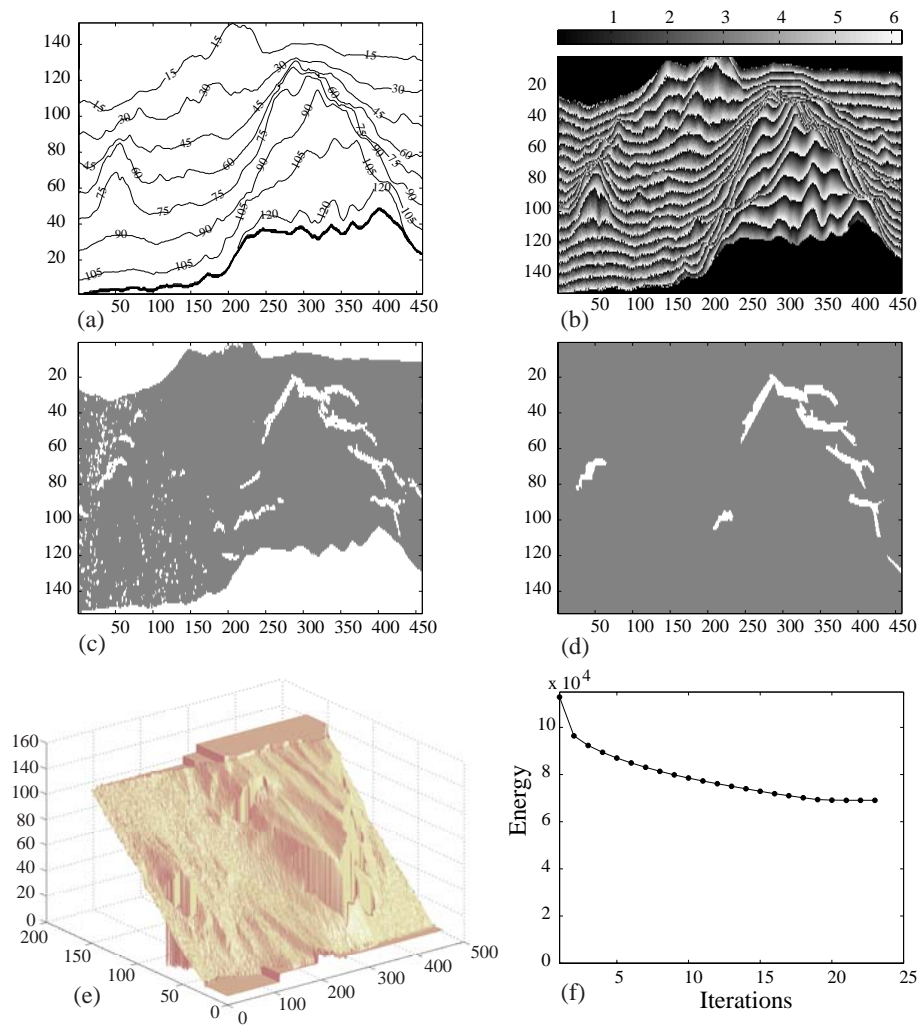


Figure 5.5: (a) Contour map (values in radians) corresponding to the Long's Peak DEM. (b) Corresponding interferogram phase image (colorbar on the top). (c) Total discontinuity information at disposal. White pixels signal discontinuity locations. (d) Discontinuity information supplied to the phase unwrapping process. White pixels signal discontinuity locations. (e) 3-D rendering of the image in (b) unwrapped in 23 iterations. (f) Energy decreasing for the unwrapping process.

Table 5.1: PUMF vs. reference PU algorithms. Phase unwrapping problems presented in section 5.1.

Algorithm	Error (radians)		
	Gaussian (Clean)	Gaussian (Noisy)	Gauss. NullQuarter (Clean)
PUMF	0	0.51	0
GBC	0	0.55	1.08
QG	0	0.60	0.36
MC	0	0.75	2.16
FMD	0	0.51	1.23
WLS	2.33	0.36	5.99
L0N	0	0.51	5.41

Table 5.2: PUMF vs. reference PU algorithms. Phase unwrapping problems presented in section 5.2.

Algorithm	Error (radians)	
	Shear Planes (Clean)	Shear Planes (Noisy)
PUMF	0	0.10
GBC	0	0.47
QG	0	6.71
MC	1.99	4.56
FMD	2.54	1.43
WLS	1.12	3.00
L0N	1.15	1.65

Table 5.3: PUMF vs. reference PU algorithms. Phase unwrapping problem presented in section 5.3.

Algorithm	Error (radians)
	Long's Peak (Clean)
PUMF	0.30
GBC	8.12
QG	12.02
MC	14.77
FMD	0.50
WLS	1.14
L0N	0.48

The obtained results clearly illustrate the competitiveness of PUMF with relation to the main state-of-the-art algorithms.

## Chapter 6

# Concluding Remarks

We have presented a new approach to the phase unwrapping problem. Our method employs energy minimization concepts, using a binary-moves optimization scheme adopted from the  $\mathbb{Z}\pi\text{M}$  algorithm [6], jointly with graph cuts techniques for binary optimization.

The proposed algorithm – the PUMF – addresses the phase unwrapping problem entirely in the integers domain, therefore handling a discrete optimization problem for which it is an exact global minimizer. It was shown that, in particular, PUMF exactly solves the minimum  $L^p$  norm PU problem, for  $p \geq 1$ . Moreover, the PUMF flexibility to admit any  $2\pi$ -periodically convex clique potential, suggests the ability to blindly deal with phase discontinuities. This was confirmed by the experiments presented, which also show the PUMF competitiveness with state-of-the-art algorithms.

Addressing non-convex potentials can be an interesting extension of the current work. Such potentials are well known to possess discontinuity preserving capabilities. In particular, a minimum  $L^0$  norm PU algorithm is commonly regarded as the desirable solution for phase unwrapping, yet an  $NP$ -hard problem<sup>1</sup>. This leads, then, to research on suitable approximate optimization techniques, which may, possibly, have the additional benefit of speeding up, even more, the PUMF algorithm.

---

<sup>1</sup>All the minimum  $L^p$  norm problems with  $p \leq 1$  are NP-Hard [45].

# Appendix A

## Proof of Theorem 1

This proof parallels the proofs of Lemma 1 in the appendixes of [6] and of [40], with the appropriate modifications to deal with the more general clique potentials here employed.

Define  $\Delta k_{ij} = [k_2]_{ij} - [k_1]_{ij}$ , for  $(i, j) \in \mathbb{Z}_0$  where  $\mathbb{Z}_0 = \{(i, j) : i = 1, \dots, M, j = 1, \dots, N\}$ , with  $M$  and  $N$  denoting the number of lines and columns respectively (i.e., the usual image pixel indexing 2D grid). Given that the energy  $E(\mathbf{k}|\boldsymbol{\psi})$  depends only on differences between elements of  $\mathbf{k}$ , we take  $\Delta k_{ij} \geq 0$  for  $(i, j) \in \mathbb{Z}_0$ . Define  $n = \max_{ij}(\Delta k_{ij})$  and the wrap-count image sequence  $\{\mathbf{k}^{(t)}, t = 0, \dots, n\}$ , such that  $\mathbf{k}^{(0)} = \mathbf{k}_1$ ,  $\mathbf{k}^{(n)} = \mathbf{k}_2$ , and

$$k_{ij}^{(t)} = k_{ij}^{(0)} + \min(t, \Delta k_{ij}), t = 0, \dots, n. \quad (\text{A.1})$$

The energy variation  $\Delta E \equiv E(\mathbf{k}_2|\boldsymbol{\psi}) - E(\mathbf{k}_1|\boldsymbol{\psi})$  can be decomposed as

$$\Delta E \equiv \sum_{t=1}^n \underbrace{\left[ E(\mathbf{k}^{(t)}|\boldsymbol{\psi}) - E(\mathbf{k}^{(t-1)}|\boldsymbol{\psi}) \right]}_{\Delta E^{(t)}}.$$

Since  $\Delta E < 0$  by hypothesis, then at least one of the terms  $\Delta E^{(t)}$  of the above sum is negative. The theorem is proved if we show that the variation  $\delta E^{(t)} \equiv E(\mathbf{k}^{(0)} + \delta \mathbf{k}^{(t)}|\boldsymbol{\psi}) - E(\mathbf{k}^{(0)}|\boldsymbol{\psi})$  satisfies  $\delta E^{(t)} \leq \Delta E^{(t)}$ , where  $\delta \mathbf{k}^{(t)} \equiv \mathbf{k}^{(t)} - \mathbf{k}^{(t-1)}$ , for any  $t = 1, \dots, n$ . This condition is equivalent to

$$0 \leq E(\mathbf{k}^{(t)}|\boldsymbol{\psi}) - E(\mathbf{k}^{(t-1)}|\boldsymbol{\psi}) - E(\mathbf{k}^0 + \mathbf{k}^{(t)} - \mathbf{k}^{(t-1)}|\boldsymbol{\psi}) + E(\mathbf{k}^0|\boldsymbol{\psi}), \quad (\text{A.2})$$

for  $t = 1, \dots, n$ . Introducing (4.1) into (A.2), we obtain  $0 \leq S^h + S^v$ , where

$$S^h = \sum_{ij} \left[ V \left( \Delta \phi_{ij}^{h(t)} \right) - V \left( \Delta \phi_{ij}^{h(t-1)} \right) + V \left( \Delta \phi_{ij}^{h(0)} \right) - V \left( \Delta \phi_{ij}^{h(0)} + \Delta \phi_{ij}^{h(t)} - \Delta \phi_{ij}^{h(t-1)} \right) \right] \bar{v}_{ij} \quad (\text{A.3})$$

$$S^v = \sum_{ij} \left[ V \left( \Delta \phi_{ij}^{v(t)} \right) - V \left( \Delta \phi_{ij}^{v(t-1)} \right) + V \left( \Delta \phi_{ij}^{v(0)} \right) - V \left( \Delta \phi_{ij}^{v(0)} + \Delta \phi_{ij}^{v(t)} - \Delta \phi_{ij}^{v(t-1)} \right) \right] \bar{h}_{ij}, \quad (\text{A.4})$$

where  $V$  is the clique potential, and  $\Delta \phi_{ij}^{h(t)}$  and  $\Delta \phi_{ij}^{v(t)}$  are given by (4.2) and (4.3), respectively, computed at the wrap-count image  $\mathbf{k}^{(t)}$ . To prove (A.2), we now show that the terms of  $S^h$  corresponding to a given site  $(i, j) \in \mathbb{Z}_1$  have positive sum. The same is true concerning  $S^v$ .

The difference  $k_{ij}^{(t)} - k_{ij-1}^{(t)}$ , for  $t = 0, \dots, n$ , is a monotone sequence. This is a consequence of the definition (A.1): if  $\Delta k_{ij} > \Delta k_{ij-1}$  the sequence is monotone increasing; if  $\Delta k_{ij} \leq \Delta k_{ij-1}$  the sequence is monotone decreasing. Therefore the sequence  $\left\{ \Delta \phi_{ij}^{h(t)} \right\}$ , for  $t = 0, \dots, n$ , is also monotone. Define  $a \equiv \Delta \phi_{ij}^{h(0)}$ ,  $b \equiv \Delta \phi_{ij}^{h(t-1)}$ , and  $c \equiv \Delta \phi_{ij}^{h(t)}$ , and without loss of generality let us assume<sup>1</sup>  $a \geq b \geq c$ . We will show that the sum of terms of  $S^h$ , corresponding to the site  $(i, j)$  is positive:

$$\begin{aligned} V(c) - V(b) + V(a) - V(a + c - b) &\geq 0 \\ V(a) + V(c) - V(b) &\geq V(a + c - b). \end{aligned} \quad (\text{A.5})$$

By hypothesis,  $V$  is convex. Also by hypothesis,  $a \geq b \geq c$ , so  $\exists t \in [0, 1] : b = at + c(1 - t)$ . Thus,

$$V(b) \leq tV(a) + (1 - t)V(c) \quad (\text{A.6})$$

$$V(a) + V(c) - V(b) \geq V(a) + V(c) - [tV(a) + (1 - t)V(c)] \quad (\text{A.7})$$

$$\geq (1 - t)V(a) + tV(c). \quad (\text{A.8})$$

---

<sup>1</sup>The only possibilities are either  $a \geq b \geq c$  or  $a \leq b \leq c$ , because the sequence  $\left\{ \Delta \phi_{ij}^{h(t)} \right\}$  is monotone as we have shown.

As  $V$  is convex,  $(1-t)V(a) + tV(c) \geq V[(1-t)a + tc]$ . So, from (A.8),

$$V(a) + V(c) - V(b) \geq V[(1-t)a + tc] \tag{A.9}$$

$$\geq V(a + c - \underbrace{[at + c(1-t)]}_b) \tag{A.10}$$

$$\geq V(a + c - b). \tag{A.11}$$

The same reasoning applies to  $S^v$ .

■

# Bibliography

- [1] P. Rosen, S. Hensley, I. Joughin, F. LI, S. Madsen, E. Rodriguez, and R. Goldstein. Synthetic aperture radar interferometry. *Proceedings of the IEEE*, 88(3):333–382, March 2000.
- [2] R. Bamler, M. Eineder, B. Kampes, H. Runge, and N. Adam. SRTM and Beyond: Current Situation and New Developments in Spaceborne InSAR. In *Proceedings of the Joint IS-PRS/EARSeL Workshop: High Resolution Mapping From Space 2003, Hannover, Germany*, 2003.
- [3] R. Gens. Two-dimensional phase unwrapping for radar interferometry: developments and new challenges. *International Journal of Remote Sensing*, 24(4):703–710, 2003.
- [4] G. Franceschetti and R. Lanari. *Synthetic Aperture Radar Processing*. CRC Press, 1999.
- [5] C. Werner, U. Wegmuller, and T. Strozzi. Processing strategies for phase unwrapping for InSAR applications. In *EUSAR'02 European Conference on Synthetic Aperture Radar*, Cologne, June 2002.
- [6] J. Dias and J. Leitão. The  $\mathbb{Z}\pi\text{M}$  algorithm for interferometric image reconstruction in SAR/SAS. *IEEE Transactions on Image Processing*, 11:408–422, April 2002.
- [7] V. Kolmogorov and R. Zabih. What energy functions can be minimized via graph cuts? *IEEE Transactions on Pattern Analysis and Machine Intelligence*, 26(2):147–159, February 2004.
- [8] T. Lillesand and R. Kiefer. *Remote Sensing and Image Interpretation*. John Wiley & Sons, 2000.
- [9] C. Elachi. *Spaceborne Radar Remote Sensing: Applications and Techniques*. IEEE Press, New York, 1988.
- [10] J. Bioucas-Dias. Radar imaging. Radar Imaging class notes (graduate course given at IST), 2005.
- [11] M. Soumekh. *Synthetic Aperture Radar Signal Processing with MATLAB algorithms*. Wiley-Interscience, 1999.

- [12] R. Chatterjee. *Antenna Theory and Practice*. New Age International Pvt Ltd, New York, 2004.
- [13] S. Buckreuss, W. Balzer, P. Mhlbauer, R. Werninghaus, and W. Pitz. The TerraSAR-X Satellite Project. In *Proceedings of the 2003 International Geoscience and Remote Sensing Symposium-IGARSS'03*, Toulouse, 2003.
- [14] A. Rogers and R. Ingalls. Venus: Mapping the surface reflectivity by radar interferometry. *Science*, 165:797–799, 1969.
- [15] S. Zisk. A new earth-based radar technique for the measurement of lunar topography. *Moon*, 4:296–300, 1972.
- [16] L. Graham. Synthetic interferometer radar for topographic mapping. *Proceedings of the IEEE*, 62(2):763–768, 1974.
- [17] C. Jakowatz, D. Wahl, P. Eichel, D. Ghiglia, and P. Thompson. *Spotlight-Mode Synthetic Aperture Radar: A Signal Processing Approach*. Kluwer Academic Publishers, Boston, 1996.
- [18] G. Crow, E. Crow, and M. Crow. *Statistics Manual*. Courier Dover Publications, 1960.
- [19] R. Bamler and P. Hartl. Synthetic aperture radar interferometry. *Inverse Problems*, 14:R1–R54, 1998.
- [20] F. Amelung, D. Galloway, J. Bell, H. Zebker, and R. Laczniak. Sensing the ups and downs of las vegas: Insar reveals structural control of land subsidence and aquifer-system deformation. *Geology*, 27(6):483–486, June 1999.
- [21] R. Romeiser, H. Breit, M. Eineder, H. Runge, P. Flament, K. de Jong, and J. Vogelzang. Current measurements by sar along-track interferometry from a space shuttle. *IEEE Transactions on Geoscience and Remote Sensing*, 43(10):2315–2324, October 2005.
- [22] T. Silva. Interferometria de imagens de radar de abertura sintética. Algoritmos e aplicações. Master's thesis, Instituto Superior Técnico, Lisboa, 2002.
- [23] P. Kelly, H. Derin, and K. Hartt. Adaptive segmentation of speckled images using a hierarchical random field model. *IEEE Trans. Acoust. Speech Signal Process.*, 38(10):1628–1641, 1988.
- [24] E. Rodriguez and J. Martin. Theory and design of interferometric synthetic aperture radars. *IEE Proceedings-F*, 139:147–159, 1992.
- [25] K. Miller and M. Rochewarger. A covariance approach to spectral moment estimation. *IEEE Trans. Inform. Theory*, IT-18(5):588–596, Sep. 1972.

- [26] J. Hadamard. Sur les problèmes aux dérivées partielles et leur signification physique. *Princeton University Bulletin*, (13), 1902.
- [27] K. Itoh. Analysis of the phase unwrapping problem. *Applied Optics*, 21(14), 1982.
- [28] T. Walker and J. Walker. *Fourier Analysis*. Oxford University Press US, 1988.
- [29] D. Ghiglia, G. Mastin, and L. Romero. Cellular automata method for phase unwrapping. *Journal of the Optical Society of America*, 4(1):267–280, 1987.
- [30] R. Goldstein, H. Zebker, and C. Werner. Satellite radar interferometry: Two-dimensional phase unwrapping. In *Symposium on the Ionospheric Effects on Communication and Related Systems*, volume 23, pages 713–720. Radio Science, 1988.
- [31] D. Ghiglia and M. Pritt. *Two-Dimensional Phase Unwrapping. Theory, Algorithms, and Software*. John Wiley & Sons, New York, 1998.
- [32] J. Huntley. Noise-immune phase unwrapping algorithm. *Applied Optics*, 28(15):3268–3270, 1989.
- [33] R. Cusack, J. Huntley, and H. Goldrein. Improved noise-immune phase unwrapping algorithm. *Applied Optics*, 34(5):781–789, 1995.
- [34] M. Roth. Phase unwrapping for interferometric SAR by the least-error path. Technical report, Johns Hopkins University Applied Physics Lab Technical Report, Laurel, MD, 1995.
- [35] H. Lim, W. Xu, and X. Huang. Two new practical methods for phase unwrapping. In *Proceedings of the 1995 International Geoscience and Remote Sensing Symposium-IGARSS'95*, pages 196–198, 1995.
- [36] C. Prati, M. Giani, and N. Leuratti. SAR interferometry: A 2-D phase unwrapping technique based on phase and absolute values information. In *Proceedings of the 1990 International Geoscience and Remote Sensing Symposium-IGARSS'90*, pages 2043–2046, 1990.
- [37] D. Derauw. Phase unwrapping using coherence measurements. *Synthetic Aperture Radar and Passive Microwave Sensing, Proceedings SPIE*, 2584:319–324, 1995.
- [38] T. Flynn. Consistent 2-D phase unwrapping guided by a quality map. In *Proceedings of the 1996 International Geoscience and Remote Sensing Symposium-IGARSS'96*, volume 4, pages 2057–2059, Lincoln, NE, 1996.
- [39] B. Reddy. *Introductory Functional Analysis*, volume 27 of *Texts in Applied Mathematics Series*. Springer-Verlag, New York, 1997.

- [40] T. Flynn. Two-dimensional phase unwrapping with minimum weighted discontinuity. *Journal of the Optical Society of America A*, 14(10):2692–2701, 1997.
- [41] D. Fried. Least-squares fitting a wave-front distortion estimate to an array of phase-difference measurements. *Journal of the Optical Society of America*, 67(3):370–375, 1977.
- [42] R. Hudgin. Wave-front reconstruction for compensated imaging. *Journal of the Optical Society of America*, 67(3):375–378, 1977.
- [43] D. Ghiglia and L. Romero. Robust two-dimensional weighted and unweighted phase unwrapping that uses fast transforms and iterative methods. *Journal of the Optical Society of America A*, 11:107–117, 1994.
- [44] M. Costantini. A novel phase unwrapping method based on network programming. *IEEE Transactions on Geoscience and Remote Sensing*, 36(3):813–821, May 1998.
- [45] C. Chen. *Statistical-Cost Network-Flow Approaches to Two-Dimensional Phase Unwrapping for Radar Interferometry*. PhD thesis, Stanford University, 2001.
- [46] M. Garey and D. Johnson. *Computers and Intractability : A Guide to the Theory of NP-Completeness*. Series of Books in the Mathematical Sciences. W. H. Freeman, New York, 1979.
- [47] C. Chen and H. Zebker. Network approaches to two-dimensional phase unwrapping: intractability and two new algorithms. *Journal of the Optical Society of America*, 17(3):401–414, 2000.
- [48] J. Leitão and M. Figueiredo. Absolute phase image reconstruction: A stochastic non-linear filtering approach. *IEEE Transactions on Image Processing*, 7(6):868–882, June 1997.
- [49] J. Dias and J. Leitão. Simultaneous phase unwrapping and speckle smoothing in SAR images: A stochastic nonlinear filtering approach. In *EUSAR'98 European Conference on Synthetic Aperture Radar*, pages 373–377, Friedrichshafen, May 1998.
- [50] M. Datcu and G. Palubinskas. Multiscale bayesian height estimation from insar using a fractal prior. In *SAR Image Analysis, Modelling, and Techniques, Proceedings of the SPIE*, pages 155–163, Bellingham, WA, 1998. Society of Photo-Optical Instrumentation Engineers.
- [51] B. Friedlander and J. Francos. Model based phase unwrapping of 2-d signals. *IEEE Transactions on Signal Processing*, 44(12):2999–3007, 1996.
- [52] D. Greig, B. Porteous, and A. Seheult. Exact maximum a posteriori estimation for binary images. *Journal of Royal Statistics Society B*, 51(2):271–279, 1989.

- [53] O. Veksler. *Efficient Graph-Based Energy Minimization Methods In Computer Vision*. PhD thesis, Cornell University, 1999.
- [54] Y. Boykov, O. Veksler, and R. Zabih. Fast approximate energy minimization via graph cuts. *IEEE Transactions on Pattern Analysis and Machine Intelligence*, 23(11):1222–1239, 2001.
- [55] P. Ferrari, M. Gubitoso, and E. Neves. Reconstruction of gray-scale images. *Methodology and Computing in Applied Probability*, 3:255–270, 2001.
- [56] Z. Wu and R. Leahy. An optimal graph theoretic approach to data clustering: Theory and its application to image segmentation. *IEEE Transactions on Pattern Analysis and Machine Intelligence*, 15(11):1101–1113, November 1993.
- [57] H. Ishikawa. Exact optimization for markov random fields with convex priors. *IEEE Transactions on Pattern Analysis and Machine Intelligence*, 25(10):1333–1336, October 2003.
- [58] Y. Boykov and V. Kolmogorov. An experimental comparison of min-cut/max-flow algorithms for energy minimization in vision. *IEEE Transactions on Pattern Analysis and Machine Intelligence*, 26(9):1124–1137, 2004.
- [59] D. Bertsekas. *Network Optimization: Continuous and Discrete Models*. Athena-Scientific, 1998.
- [60] A. Goldberg and R. Tarjan. A new approach to the maximum-flow problem. *Journal of the Association for Computing Machinery*, 35(4):921–940, October 1988.
- [61] H. Lim, W. Xu, and X. Huang. Two new practical methods for phase unwrapping. In *Proceedings of the 1995 International Geoscience and Remote Sensing Symposium-IGARSS'95*, pages 196–198, Firenze, Italy, 1995.